Investigating the emergence of circadian clock-mediated therapeutic windows in the cell cycle of cancer cells

A thesis
Submitted towards the partial fullfilment of
BS-MS dual degree programme
by

SHAIKH ARSH YUSUF

Date: March 15, 2024

under the guidance of

DR SHAON CHAKRABARTI

National Centre for Biological Sciences

from May 2023 to March 2024

Indian Institute of Science Education and Research
Pune

Certificate

This is to certify that this dissertation entitled "Investigating the emergence of circadian clock-mediated therapeutic windows in the cell cycle of cancer cells" submitted towards the partial fulfillment of the BS-MS degree at the Indian Institute of Science Education and Research, Pune represents original research carried out by Shaikh Arsh Yusuf at the National Centre for Biological Sciences, under the supervision of Dr Shaon Chakrabarti during academic year May 2023 to March 2024.

Shaon Chakrabarti

Supervisor:
Dr Shaon Chakrabarti
Faculty
National Centre for Biological Sciences

Arsh

Shaikh Arsh Yusuf
20191115
BS-MS
IISER Pune
Date: 15/03/2024

Declaration

I, hereby declare that the matter embodied in the report titled "Investigating the emergence of circadian clock-mediated therapeutic windows in the cell cycle of cancer cells" is the result of the investigations carried out by me at the "National Centre for Biological Sciences" from the period 07-05-2023 to 31-03-2024 under the supervision of Dr Shaon Chakrabarti and the same has not been submitted elsewhere for any other degree.

Shaon Chakrabarti

Supervisor:
Dr Shaon Chakrabarti
Faculty
National Centre for Biological Sciences

Arsh

Shaikh Arsh Yusuf
20191115
BS-MS
IISER Pune
Date: 15/03/2024

Acknowledgements

I would like to thank Dr Shaon Chakrabarti for providing me with the necessary resources and the space to shape this project independently. I am grateful to my lab mates for creating a space where I could address my question using a combination of mathematical and biological tools. Of particular mention is Vishnupriya Arulanandan, who not only helped me freeze cell lines and perform time point-based experiments but was also an audience to my mini-lecture series, wherein I formulated my plans to address each subgoal of this project. I would like to thank Krishnamurthy H, who helped us generate the flow cytometry data.

I would like to thank my funders for supporting me financially. I would like to thank the Simons Centre for Living Machines, which funded my stay at NCBS. I would like to thank Kishor Vaigyanik Protsahan Yojana (KVPY) and Infosys Foundation Scholarship for supporting my tuition fees.

Contributions

Contributor name	Contributor role
Shaon Chakrabarti, Arsh Shaikh	Conceptualization Ideas
Arsh Shaikh, Anjoom Nikhat, Shaon Chakrabarti	Methodology
Arsh Shaikh	Software
Arsh Shaikh	Validation
Arsh Shaikh, Krishnamurthy H	Formal analysis
Arsh Shaikh, Vishnupriya Arulanandan	Investigation
Shaon Chakrabarti	Resources
NA	Data Curation
Arsh Shaikh, Vishnupriya Arulanandan	Writing - original draft preparation
NA	Writing - review and editing
Arsh Shaikh	Visualization
Shaon Chakrabarti	Supervision
Shaon Chakrabarti	Project administration
Shaon Chakrabarti	Funding acquisition

Abstract

The circadian cycle is an approximately 24-hour cycle of physiological and biochemical processes in organisms. At a cellular level, the circadian clock comprises core clock genes showing oscillatory expression with a period of nearly 24 hrs These genes directly regulate cell cycle checkpoints. The clock-cell cycle coupling is crucial to cancer therapy since it has been shown that the maximum tolerated dose and the treatment outcome in cancer chemotherapy and radiotherapy differ depending on the dosage time. Chronotherapy is an emerging cancer therapy scheme wherein patients are administered therapy based on their circadian cycles. However, a proper understanding of the coupling of the clock to the cell cycle in different cancer cells and the effect of therapy on these oscillators is needed before we can apply chronotherapy on a large scale.

In my thesis, I developed an agent-based four-compartment simulation based on the stochastic molecular clock and cell cycle gene dynamics, which can simulate cell proliferation and recapitulate physically realistic cell cycle phase durations. I further introduced a modified Linear-Quadratic (LQ) model that describes the dose and cell cycle phase-dependent effect of radiation on cells. I use HCT116 cells to experimentally show that clock coupling to the cell cycle can lead to a roughly 25.8 hr oscillation in the G_1 proportion. Using the radiation simulation, I show that circadian coupling to cell cycles opens a therapeutic window wherein we can target specific cell types at their most sensitive cell cycle phase. The radiation model further suggests that daily dosing would not be an optimal therapy scheme due to post-radiation cell cycle arrest.

We can use the radiation model to understand the effect of irradiating cells at different times, allowing us to develop an optimal sequential chronotherapy scheme for cancer.

Contents

Chapter 1

Introduction

The circadian cycle is an approximately 24-hour cycle of physiological and biochemical processes in organisms. The physiology of the circadian clock in different species is different. However, they share common features, like being self-sustained oscillations that environmental cues like sunlight, temperature, etc., can entrain. Plants and animals show circadian patterns in their behavior. For example, diurnal animals sleep at night while nocturnal ones wake up. Before dawn, plants position their leaves in the direction of sunrise. Besides behavioral patterns, the circadian clock regulates physiological phenomena like body temperature, blood pressure, hormones, metabolism, etc., (Buhr and Takahashi, 2013). At a cellular level, the circadian cycle regulates cell proliferation. It is, thus, not surprising that circadian disruption leads to cancer (Lee (2021), Shafi and Knudsen (2019)). Understanding the coupling between the circadian clock and cell proliferation can aid us in understanding tumorigenesis and refine current therapy schemes to be more effective.

Chronotherapy is an emerging therapy scheme that modulates drug or radiation dosage depending on the patient's circadian cycle. Clinical trials using chronotherapy show that it can reduce toxicity and increase treatment tolerability (Lévi, 2002). However, the applicability of chronotherapy is restricted due to a poor understanding of the difference in the proliferation of cancer and normal cells when coupled to the same circadian clock in a patient. Furthermore, it is not well understood how therapy can affect the circadian cycle in a patient, making sequential dosing in chronotherapy a challenge.

In this thesis, I used an interdisciplinary approach to understand the effect of radiation therapy on a population of clock-coupled cells. I describe a four-compartment lineage-generating model that I developed, which simulates the dynamics of the molecular clock and cell cycle regulators, and cell proliferation. Using this model, I have further developed a radiation

simulation that can help us understand the effect of radiotherapy on proliferating cells. The radiation simulation can be used to study different dosing strategies and their effect on cancer proliferation and normal cell death.

1.1 The mammalian circadian clock

In mammals, circadian cycles are maintained at cellular, tissue, and organ level. The central pacemaker in mammals is located in the hypothalamus's suprachiasmatic nucleus (SCN) (Fig 1.1) (Welsh *et al.*, 2010). The SCN regulates daily cycles of temperature, hunger, sleep, etc. The SCN is entrained by photic inputs sensed by special photosensitive retinal cells that project into it via the retinohypothalamic tract (Welsh *et al.*, 2010). The SCN synchronizes the other oscillators in the body via direct neuronal pathways or hormonal regulation. It also has less direct ways to regulate the body's clock, like varying body temperature, feeding behavior, etc.

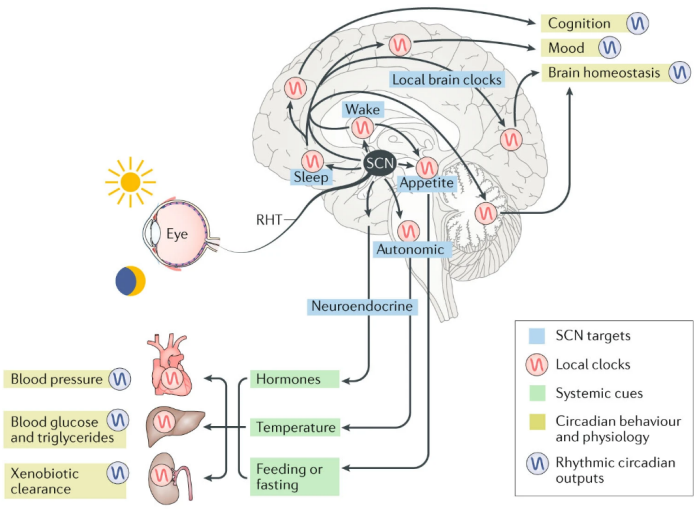

Figure 1.1: A schematic of the SCN and its connection to the peripheral tissues. The SCN is synchronized by photic inputs from the retina and in turn, synchronizes the peripheral tissue. The local clocks in the peripheral tissue lead to circadian patterns in physiological processes like blood pressure, renal function, etc. Image taken from Hastings *et al.* (2018).

In 1998, Balsalobre *et al.* (1998) observed that shocking rat fibroblasts and hepatoma cells with serum led to circadian cycling of clock genes like *Per1*, *Per2*, *Rev-erbα*, etc. These sustained oscillations persisted even when the cells were grown in a serum-free medium after the serum shock with a

period of 22.5 ± 1.7 hrs. Furthermore, they observed that serum shock in hepatoma cells induced the same response as light synchronization in SCN neurons. This led to the discovery of peripheral clocks located in most of our peripheral tissues, like the liver, skin, lung, heart, etc., capable of generating circadian rhythms independently. Yoo *et al.* (2004) used *Per2::Luc* knock-in mice and found that while peripheral clocks can independently generate sustained circadian oscillations, in the absence of SCN, they all desynchronize at a tissue level.

Thus, the mammalian circadian network is hierarchical, with the SCN synchronizing the peripheral clocks and the peripheral clocks synchronizing cellular functions at a tissue level.

1.2 The molecular clock network

At the cellular level, the circadian clock comprises of two negative feedback loops that generate 24-hour rhythms (Fig 1.3) (Relógio *et al.* (2011),Ko and Takahashi (2006)). The core clock genes are *Bmal1* (Brain and Muscle *Arnt1* like), its paralogue neuronal PAS domain protein 2 (*Npas2*) and *Clock* (short for circadian locomotor output cycles kaput). During the day, these genes code for transcriptional activators that heterodimerize and bind to the E-box *cis*- elements in the promoters of other clock genes like period homologs (*Per1*, *Per2*, and *Per3*) and the Cryptochrome (*Cry1* and *Cry2*). These genes get transcribed and translated during the day and undergo post-translational modifications. During the night, the resultant PER and CRY proteins heterodimerize and translocate to the nucleus, where they repress their own production, completing the negative feedback loop. This entire loop takes 24 hours to cycle once.

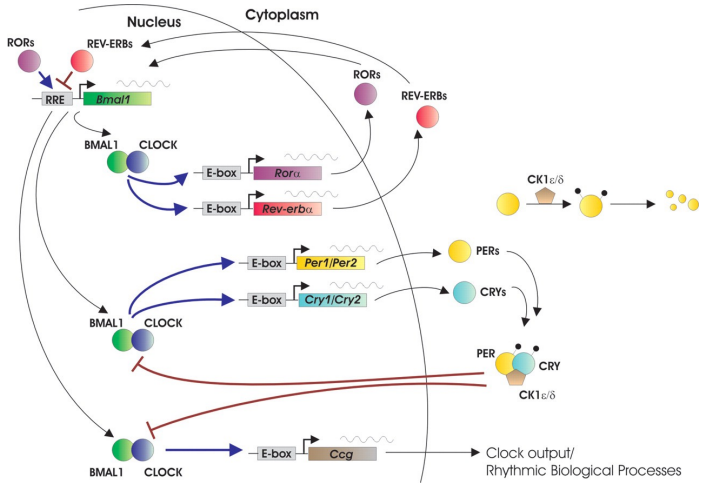

Figure 1.2: A schematic of the clock transcription-translational feedback loop (TTFL). Image taken from Ko and Takahashi (2006).

The BMAL1/CLOCK heterodimer also binds to the E-box of retinoic acid-related orphan receptor (*Rora*, *Rorb*, *Rorc*) and *Rev-Erb* nuclear orphan receptor (*Rev-Erbα*, *Rev-Erbβ*) activating their transcription during the day. The ROR and REV-ERB proteins bind to the retinoic acid-related orphan receptor response elements (ROREs) present in the promoter region of *Bmal1*. RORs promote *Bmal1* transcription while REV-ERBs inhibit it.

The BMAL1/CLOCK-PER/CRY negative feedback loop is the main loop that sets up the cellular clock. However, the role of the RORs and REV-ERBs is not entirely understood in maintaining the circadian rhythm. Work by Liu *et al.* (2008) showed that the circadian clock showed normal oscillations even in $Rorc^{-/-}$ mice, suggesting redundancy in the second circadian loop. However, the RORs and REV-ERBS are thought to stabilize the clock and make it robust. BMAL1/CLOCK can bind to the E-box regulatory elements of various genes involved in other biological processes, leading to circadian oscillations in cellular activity.

1.3 Coupling between the clock and the cell cycle

The cell cycle is regulated by cyclins and cyclin-dependent kinases (CDKs), which interact with each other and dictate the transition of cells across cell cycle phases. Progression through the G_1, S, G_2, and G_2/M is controlled by Cyclin D/CDK4–6, Cyclin E/CDK2, Cyclin A/CDK2 and Cyclin B/CDK1, respectively (Yan and Goldbeter, 2019). Cyclin-B-Cdc2/CDK1 complex is also known as the Maturation Promoting Factor (MPF) as it acts as a mitotic inducer in eukaryotic cells. However, work by Hara *et al.* (2012). showed that Cyclin B/CDK1 alone cannot act as an M-phase promoter. Transition to the M phase also requires another kinase called the Greatwall kinase that suppresses the protein phosphatase 2A-B55, which opposes cyclin B–Cdk1 (Hara *et al.*, 2012). M phase entry is also regulated by a kinase called WEE1, which phosphorylates specific residues of CDK1, inhibiting its binding to Cyclin-B and preventing premature mitosis.

Various experiments have highlighted that the clock is coupled to the cell cycle (Gaucher *et al.*, 2018), particularly at the G_1/S and G_2/M transitions. The G_1 to S transition is regulated by transcriptional control of the genes *p21* and *p16*. *p21* inhibits the cell cycle by binding to various cyclin-CDK complexes. The clock genes ROR and REV-ERB compete to bind the RORE site located in the *p21* and inhibit its transcription. *p16* binds to Cyclin D/CDK4–6 complex and prevents G_1/S transition. PER regulates *p16* via a multifunctional nucleoprotein called NONO (Kowalska *et al.*, 2013). At the G_2/M checkpoint, the BMAL/CLOCK complex binds to the E-box of the gene *Wee1* and increases its transcription, preventing entry into mitosis.

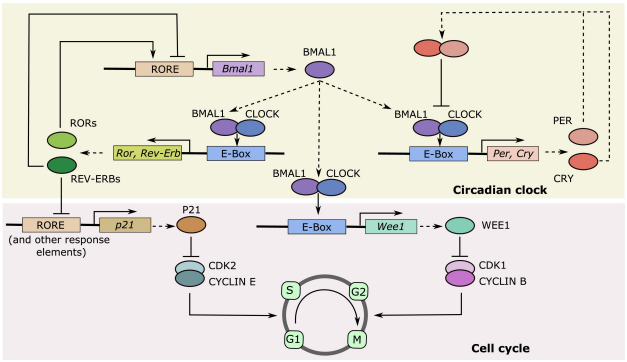

Figure 1.3: A schematic of the cell cycle regulation by the clock. Image taken from Chakrabarti and Michor (2020).

It is currently unclear if the cell cycle also affects the clock dynamics.

Matsuo *et al.* (2003), who discovered the coupling between BMAL/CLOCK and *Wee1*, also showed that cell cycle block in mouse hepatocyte cells did not affect the circadian oscillation of PER2. However, some of the earliest evidence of the cell cycle machinery affecting clock genes comes from Oklejewicz *et al.* (2008), who noted the link between DNA damage response pathways linked to *Per2* gene expression. Miki *et al.* (2013) showed that the transcription factor *p53* competes with BMAL1/CLOCK in binding to the *Per2* promoter. However, the reverse coupling is not fully characterized at a molecular level, with Bieler *et al.* (2014) claiming that only unidirectional coupling exists from the cell cycle to the clock in NIH3T3 cells, while Feillet *et al.* (2015) claim that the coupling is bidirectional.

1.4 Mathematical models for the circadian clock and the cell cycle

The earliest mathematical model for the circadian clock came from a modified version of the Goodwin oscillator model (Ruoff and Rensing, 1996). With growing research in *Drosophila* circadian rhythms, Goldbeter gave a minimal model of 5 equations to model the circadian cycle of PER (Goldbeter, 1995). Since then, several models have looked at the circadian clock of different organisms, including mammals.

Mammalian circadian clock models either describe the molecular details of the clock TTFL or the population oscillations of cells under circadian rhythm without using any molecular details. Becker-Weimann *et al.* (2004) gave a mathematical model consisting of 7 ODEs that describe the dynamics of the core clock network. They take into account the three conditions that an oscillator must satisfy (Friesen and Block, 1984)-

1. A source of excitation
2. A restorative process
3. A source of delay

The clock network modeled by Becker-Weimann *et al.* (2004) is shown in Fig 1.4. Apart from the feedback loops obtained from experiments, the delay in their model comes from prescription, translation, and nuclear transport. Their model could generate circadian patterns in the cell cycle components, having experimentally agreeable phase shifts between different components.

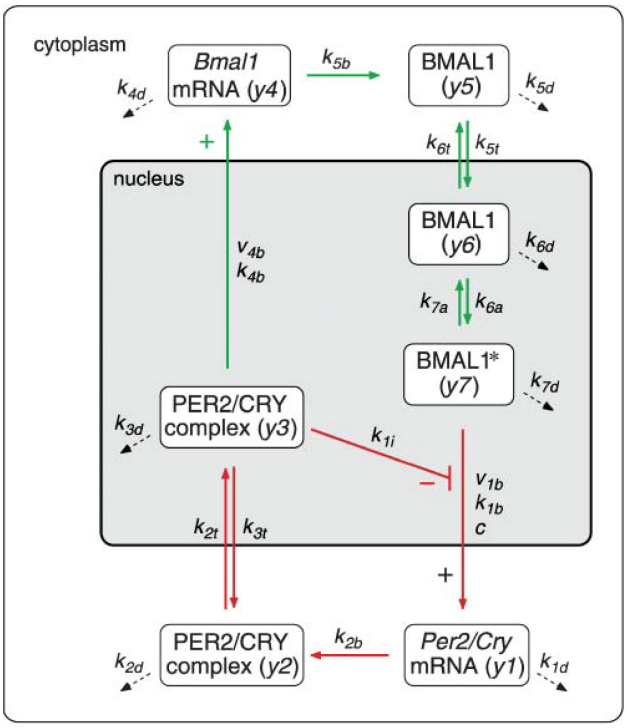

Figure 1.4: A schematic of the clock network modeled by Becker-Weimann *et al.* (2004). Image taken from Becker-Weimann *et al.* (2004).

Modeling the cell cycle requires a careful understanding of the complex interaction of the Cyclins and CDKs. Tyson and Novak (2001) gave one of the earliest detailed models for the cell cycle by noticing that at the root of the cell cycle oscillator was the antagonistic interaction between CyclinB/CDK1 and the Anaphase Promoting Complex (APC). They noted hysteresis in the CyclinB-APC loop, wherein a cell marked for division cannot revert back. While they initially gave a model with 8 differential equations for various cell cycle component dynamics, they later extended their model to have 13 components to describe the cell division in yeast (Novak *et al.*, 2001). However, their model did not involve the effect of clock coupling on the cell cycle.

Various mathematical models have looked at the molecular details of the clock and the cell cycle (Gérard and Goldbeter (2009),Zámborszky *et al.* (2007)). In these models, the clock affects the cell cycle via gating cell cycle phases. Some other models look at the effect of clock coupling on population dynamics using cellular automata (Altinok *et al.*, 2011) or age-structured population (Clairambault *et al.*, 2011) models.

El Cheikh *et al.* (2014) aimed to combine the molecular and population-level descriptions and explain the effect of clock coupling to the cell cycle on

population dynamics. They used the circadian clock model given by Becker-Weimann *et al.* (2004) and combined it with the cell cycle description of Novak *et al.* (2001).

Yan and Goldbeter (2019) have recently tried to model the molecular bidirectional coupling between the clock and the cell cycle. This model links the cell cycle to the clock via the inhibition of *Bmal1* transcription by CDK1. Understanding the molecular network for reverse coupling better will allow us to develop more accurate mathematical models that model the clock and cell cycle dynamics.

1.5 Effect of radiation on the cell cycle

Radiation leads to DNA damage by causing single or double-stranded DNA breaks. Double-stranded DNA breaks are considered to be lethal. Post-radiation, cells can attain three fates - 1. They undergo DNA repair and then divide normally 2. They show senescence, or 3. They show cell death (Reyes *et al.*, 2018). Radiation-induced DNA damage is sensed by DNA repair post-radiation can happen via homologous recombination (HR) in the S/G_2 phase or by non-homologous end joining (NHEJ) in the G_2 phase (Pawlik and Keyomarsi, 2004). Various experiments have shown that cells are least sensitive to radiation-induced DNA damage in the S phase, followed by G_1 and G_2, and most sensitive in the M phase (reviewed by Pawlik and Keyomarsi (2004)). Radiation-induced cell death can occur due to the inheritance of unrepaired DNA breaks by the progeny (necrosis) or via programmed cell death (apoptosis) (Pawlik and Keyomarsi, 2004). Maier *et al.* (2016) give a really good review of the molecular pathways involved in sensing radiation and initiating DNA damage response (DDR) pathways. However, the key point is that the tumor suppressor p53 mainly controls cell cycle arrest and apoptosis. p53 activates the transcription of *p21* which inhibits G_2/M transition. Recent work by Reyes *et al.* (2018) shows that transient fluctuations in p53 can be amplified by *p21*-CDK2 network, leading to escape from cell cycle arrest of irradiated cells. Thus, release from cell cycle arrest of surviving cells post-radiation is a stochastic process that depends on the accumulation of p53 in the nucleus and fluctuation in its levels. From a radiotherapy point of view, this raises questions on how the dosing scheme should be designed to target the cancer cells at their most vulnerable cell cycle stage.

1.6 Chronotherapy for cancer

Given the dynamic cross-talk between the circadian clock and the cell cycle, it does not come as a surprise that clock disruption can lead to various abnormalities, particularly cancer (Lee, 2021). *Bmal1/Clock* can lead to several cancers like colon cancer (Zhang *et al.*, 2020), lung adenocarcinoma (Papagiannakopoulos *et al.*, 2016), pancreatic cancer (Jiang *et al.*, 2016), etc. These cancers arise due to the effect of BMAL1/CLOCK on *p53* and *c-Myc*. Recent work by Diamantopoulou *et al.* (2022) showed that circulating tumor cells (CTCs) intravasate the most during sleep, and $Bmal^{-/-}$ mice fail to generate CTCs. Night shift workers have been shown to have higher chances of incidence of breast, colon, lung, etc (Lee, 2021).

A novel strategy to combat cancers is to use chronotherapy, a therapy scheme that targets the clock of the cancer. Sulli *et al.* (2018) categorizes chronotherapy into three categories- 1. Training the clock, 2. Clocking the drugs, and 3. Drugging the clock. While there has been a lot of research on ligands that can affect the molecular clock and lead to therapeutic effects (Sulli *et al.*, 2018), I do not discuss it below as it is out of the scope of this thesis.

1.6.1 Training the clock

Various stimuli, like light, temperature, food intake, etc, entrain the circadian cycle. By varying these stimuli, we can entrain the clock differently. In patients experiencing poor circadian cycles, behavioral therapy or sleep medication can entrain the body's circadian clock. Liu *et al.* (2016) review the use of melatonin, a hormone released by the pineal gland to promote sleep, for treating insomnia, mood disorders, and cancer.

1.6.2 Clocking the drugs

Even before the circadian network was fully understood, Hrushesky (1985) noted that switching the time of administering adriamycin and cisplatin in patients with ovarian cancer showed varied effects in dosage attenuation and patient complications. Chronotherapy has been shown to improve efficacy and reduce toxicity in mouse models (Okazaki *et al.* (2014),Takane *et al.* (2000)). Randomized multi-center clinical trials by Lévi *et al.* (1997). showed that chronotherapy with different drugs for metastatic colon cancer led to reduced drug toxicity and increased relapse time.

Chronomodulated radiotherapy relies on the radioprotective effect of the S phase of the cell cycle (Fig 1.5). The sensitivity of cells to radiation is

maximum in the M phase and the least in the late S phase (Sinclair and Morton (1965), Terasima and Tolmach (1961)). Since cancer and host cells have different cycling clocks, targeting radiotherapy at the M phase peak of cancer cells can kill more cancer cells with reduced toxic effects of radiation on host cells.

Figure 1.5: Trend in the radiosensitivity across cell cycle phases. Image taken from Plikus *et al.* (2013)

Bermúdez-Guzmán and Blanco-Saborío (2021) review some pre-clinical trials that look at chronotherapy using radiation on mouse models. Clinical trials in humans for different cancers have shown that there is a significant difference in radiation side effects and toxicity depending on the time of radiation (Harper and Talbot, 2019). However, clinical trials with head and neck cancer did not show a significant difference in patient outcomes after chronotherapy using radiation. This begs the question of how radiation affects cancer proliferation and how we can tune radiotherapy to cause maximal cancer cell death. A proper understanding of the molecular mechanisms of the clock and cell cycle and their effect on a population of cells is required to develop optimized chronotherapy strategies. Furthermore, the effect of radiation on the clock and cell cycle genes would help us devise better sequential therapy schedules.

Chapter 2

Model

2.1 Three-compartment model

El Cheikh *et al.* (2014) proposed a mathematical model that combines the molecular details of the circadian clock-cell cycle coupled oscillator system with population dynamics. The molecular dynamics of the clock genes, mRNA, and proteins were modeled using a system of seven ODEs proposed by Becker-Weimann *et al.* (2004) Fig 2.1 shows a schematic of the clock transcription-translation feedback loop.

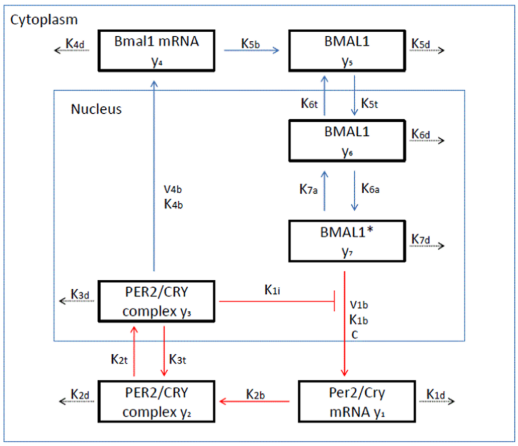

Figure 2.1: A schematic of the clock transcription-translation feedback loop modeled by El Cheikh *et al.* (2014). Image taken from El Cheikh *et al.* (2014).

The ODEs describing this network are as follows:

$$\frac{dy_1}{dt} = \frac{\nu_{1b}(y_7 + c)}{k_{1b}(1 + (\frac{y_3}{k_{1i}})^p) + y_7 + c} - k_{1d}y_1 \tag{2.1}$$

$$\frac{dy_2}{dt} = k_{2b}y_1^q - k_{2d}y_2 - k_{2t}y_2 + k_{3t}y_3 \tag{2.2}$$

$$\frac{dy_3}{dt} = k_{2t}y_2 - k_{3t}y_3 - k_{3d}y_3 \tag{2.3}$$

$$\frac{dy_4}{dt} = \frac{\nu_{4b}y_3^r}{k_{4b}^r + y_3^r} - k_{4d}y_4 \tag{2.4}$$

$$\frac{dy_5}{dt} = k_{5b}y_4 - k_{5d}y_5 - k_{5t}y_5 + k_{6t}y_6 \tag{2.5}$$

$$\frac{dy_6}{dt} = k_{5t}y_5 - k_{6t}y_6 - k_{6d}y_6 + k_{7a}y_7 - k_{6a}y_6 \tag{2.6}$$

$$\frac{dy_7}{dt} = k_{6a}y_6 - k_{7a}y_7 - k_{7d}y_7 \tag{2.7}$$

where the various variables and parameters have the same meaning as in El Cheikh *et al.* (2014).

The cell cycle model was inspired by Novak *et al.* (2001), who described the yeast cell cycle regulators using 18 ODEs. El Cheikh *et al.* (2014) considered three equations that modeled the dynamics of the Mitosis Promoting Factor (MPF) and its two antagonists, the tyrosine kinase WEE1 and the MPF inhibitor (which can be associated with the Anaphase Promoting Complex (APC)) (Fig 2.2). The ODEs (with the symbols having the same meaning as in El Cheikh *et al.* (2014)) are as follows-

$$\frac{dz_8}{dt} = \frac{k_{0mpf}k_{1mpf}^n}{k_{1mpf}^n + z_8^n + sz_{10}^n}(1 - z_8) - d_{wee1}z_9z_8 \tag{2.8}$$

$$\frac{dz_9}{dt} = \frac{k_{actw}}{k_{actw} + d_{w1}}(c_w + Cy_7) + (\frac{k_{actw}}{k_{actw} + d_{w1}} - 1)\frac{k_{inactw}z_8^n z_9}{k_{1wee1}^n + z_8^n} - d_{w2}z_9 \tag{2.9}$$

$$\frac{dz_{10}}{dt} = k_{act}(z_8 - z_{10}) \tag{2.10}$$

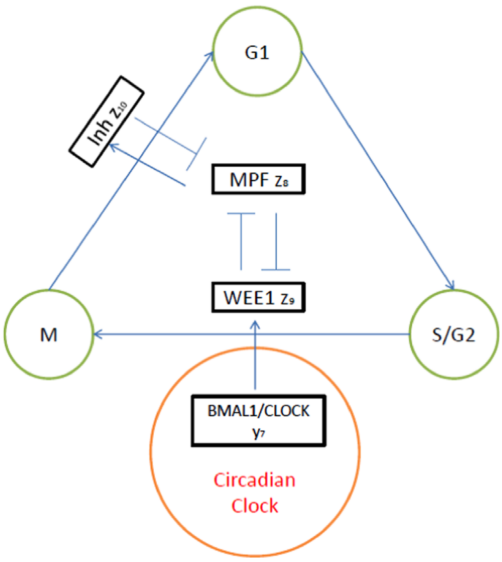

Figure 2.2: A schematic of the cell cycle model given by El Cheikh *et al.* (2014). Image taken from El Cheikh *et al.* (2014).

The coupling of the clock to the cell cycle is modeled by the coupling factor C in equation 2.9. C describes the strength of activation of the MPF by the BMAL1/CLOCK complex.

El Cheikh *et al.* (2014) used an age-structured model to model population dynamics and divided their cell cycle into three phases - G_1, S/G_2, and M. The MPF value of each cell governs the transition across the cell cycle phases. Cells transition from the G_1 to the S/G_2 phase when their MPF concentrations cross 0.09. Cells enter the M phase when their MPF activity exceeds that of WEE1. Finally, cells return to the G_1 phase when their MPF concentrations drop below 0.06.

We used the molecular dynamics model from El Cheikh *et al.* (2014). and developed our own three-compartment lineage construction simulation. We use the `igraph` package in R and construct a lineage graph with the cells as nodes and the concentrations of the clock and cell cycle components as their attributes. At every time step, we update the molecular concentrations of each cell by numerical integration of Eqns 2.1 - 2.10 and use the MPF cut-offs suggested by El Cheikh *et al.* (2014). to transition cells across the three cell cycle phases. When a cell exits the M phase to enter the G_1 phase, we replace it with two daughters having the same clock and cell cycle expression as that of the parent to simulate cell division.

While Eqns 2.1-2.10 capture the molecular oscillations of the clock and cell cycle genes, they do not model the noisy gene expression observed exper-

imentally (Elowitz *et al.* (2002), Ozbudak *et al.* (2002), Blake *et al.* (2003)). Noisy clock and cell cycle gene expression give rise to variability in the cell cycle durations across cells, and hence, incorporating it in the model is crucial to capture the effect of the clock on the cell cycle.

The concentrations of all the clock and cell cycle components are updated by Euler-Maruyama integration of Eqns 2.1-2.10 added with a noise term A given by

$$A = a_0\sqrt{\Delta t} \times \mathcal{N}(0,1) \tag{2.11}$$

where a_0 is a fixed noise amplitude, Δt is the time step, and $\mathcal{N}(0,1)$ is a random sample from a normal distribution with mean 0 and variance 1. The parameter a_0 needs to be tuned based on experimental data on the gene expression profiles of each gene included in the model. Since such data is unavailable, we used Inter-Mitotic Time (IMT) data of the human colon cancer cell line HCT116 from Chakrabarti *et al.* (2018). The IMT of HCT116 cells is best fit by an Exponentially Modified Gaussian (EMG) distribution with parameters $\mu = 14.3$, $\sigma = 2.45$ and $\lambda = 0.27$ (Chakrabarti *et al.*, 2018). The IMT captures the effect of all the clock and cell cycle components in the model and hence can be used to fix the noise amplitude (a_0). We varied a_0 and plotted the histogram of the IMT obtained from our simulation. We compared this histogram with the expected distribution predicted by the EMG distribution. We observed that a noise amplitude of 0.0025 led to a good match to the expected IMT distribution (Fig 2.3).

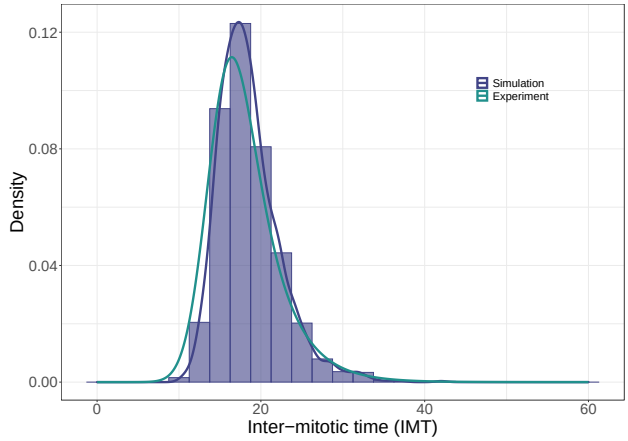

Figure 2.3: Inter-mitotic time distribution obtained from the three-compartment model when a noise of 0.0025 is added. The expected experimental value is taken from Chakrabarti *et al.* (2018)

Thus, our simulation generates a graph with the cells as nodes, the mother-daughter relationship as edges, and the clock and cell cycle expres-

sion as vertex attributes. The molecular concentrations decide the cell cycle phase of each cell. Our simulation also models the noisy expression of the genes, which gives rise to varying cell cycle durations.

2.2 Four compartment model

While the three-compartment model proposed by El Cheikh *et al.* (2014). allows us to study the effect of the clock-cell cycle coupled oscillator system at a population level, its application in chronotherapy is limited by the lack of resolution of the S/G_2 phase. We thus need a four-compartment model, with the S and G_2 phases as separate compartments, that uses the MPF concentration of a cell to assign cell cycle phases based on certain thresholds. The key objective of this thresholding is to ensure that the cell phase durations that result from it should agree with experimental trends. This is because the average fraction of cells found in a particular phase of the cell cycle at a steady state is proportional to the duration of that phase (Wheeler, 2015). Typically, the G_1 phase is the longest, followed by S, G_2, and then M. Ensuring that our model follows these trends would allow us to make better predictions on the effect of perturbations on the distribution of cells in each cell cycle phase post-irradiation. While the actual durations of the cell cycle phases can vary a lot depending on the type of cell, for a typical rapidly dividing human cell, the cell cycle durations are shown in Table 2.1.

Phase	**Expected duration (hrs)**
G_1	11
S	8
G_2	4
M	1

Table 2.1: Average cell cycle phase durations in a rapidly proliferating human cell with a total cell cycle time of 24 hours.

A straightforward approach to developing a four-compartment model would be to add an extra threshold on the MPF concentration to mark the entry into the S phase and then use the existing thresholds to assign the other cell cycle phases. The thresholds could be placed such that the average cell phase durations agree with the experimental results. This trivial approach proved to be unhelpful since thresholding alone could not solve the phase resolution problem. On careful inspection of the MPF expression profile, I realized that the time MPF takes to drop from its peak is longer than

an hour. Since MPF needs to drop below a low threshold for cell division to occur, the time that MPF takes to drop from its maximum value to its minimum would need to be adjusted in the model. Furthermore, the rise in MPF concentration during the S/G_2 phase would have to be adjusted to have a suitable rise, giving rise to appropriate cell phase durations.

The MPF concentration profile can be modified only by changing the parameterizations of the equations that determine its dynamics. Thus, in order to get the desired cell cycle phase durations, we need to understand the effect of changing each parameter in the ODEs that govern the dynamics of MPF, WEE1, and the MPF inhibitor.

2.2.1 Effect of changing the MPF parameters

The equation for the variation of the MPF concentration is (2.8)-

$$\frac{dz_8}{dt} = \frac{k_{0mpf} k_{1mpf}^n}{k_{1mpf}^n + z_8^n + s z_{10}^n}(1 - z_8) - d_{wee1} z_9 z_8$$

The production term in this equation is a modified Hill function that models the inhibitory effect of the MPF inhibitor (z_{10}) on MPF production. The degradation term simply involves the inhibitory effect that WEE1 has on MPF production. There is also an autoregulatory negative feedback loop in which MPF affects its own production and degradation. The key parameters in this equation and the effect of perturbing them are as follows:

- k_{0mpf}
  This is the maximum production rate of MPF that can be observed in the absence of any inhibitory effect of the MPF inhibitor (z_{10}). Increasing k_{0mpf} would increase the maximal MPF production rate in the simulation, leading to a rapid rise in the MPF concentration. If the degradation terms are left unchanged, this would lead to a slow drop in the MPF concentration, thus increasing the M phase duration.

- k_{1mpf}
  This parameter is the concentration of the MPF inhibitor (z_{10}) at which the production rate of MPF drops to half the maximum value (given by k_{0mpf}). Thus, increasing k_{1mpf} would delay the inhibitory effect of the MPF inhibitor on the production rate of MPF. This would rapidly increase MPF concentrations, making the G_1, S, and G_2 phases short. Changing k_{1mpf} can help us tune the time it takes for MPF to rise to its maximum.

- d_{wee1}
  This parameter controls the degradation of MPF. Increasing this parameter would cause an overall low MPF expression and a rapid drop in MPF concentration after its maximal level. This would lead to a shorter M phase.

2.2.2 Effect of changing the WEE1 parameters

The equation governing WEE1 dynamics is (2.9)-

$$\frac{dz_9}{dt} = \frac{k_{actw}}{k_{actw} + d_{w1}}(c_w + Cy_7) + (\frac{k_{actw}}{k_{actw} + d_{w1}} - 1)\frac{k_{inactw} z_8^n z_9}{k_{1wee1}^n + z_8^n} - d_{w2} z_9$$

The production term of WEE1 involves a constant production rate specified by $\frac{k_{actw}}{k_{actw}+d_{w1}}$ and its coupling between the BMAL1/CLOCK complex given by the parameter C. Note that $\frac{k_{actw}}{k_{actw}+d_{w1}}$ is always less than 1. A negative Hill function gives the degradation term, which describes the inhibitory effect of MPF on WEE1. Furthermore, there is an intrinsic degradation rate of WEE1 given by d_{w2}. The effect of perturbing some key parameters in this equation are as follows-

- k_{actw}
  This is the activation rate of WEE1 production by BMAL1/CLOCK. Changing this parameter affects both the production and the degradation term of WEE1. Thus, increasing k_{actw} would lead to more rapid WEE1 oscillations and a faster shift between the G_1 and S phase.

- d_{w1}
  This is a Michaelis constant that describes the concentration of BMAL1/CLOCK at which WEE1 production is half of its maximal value. Increasing d_{w1} would lead to a slower production rate of WEE1, which would lead to a longer G_1 phase. A lower production rate and a high degradation rate would mean that WEE1 levels drop faster, making the cell cycle's S, G_2 and M phases longer.

- c_w
  This is a constant activator concentration, which promotes the production of WEE1 even in the absence of clock coupling. Increasing c_w increases the production rate of WEE1, which in turn would increase the G_1 phase duration.

- k_{inactw}
  This is the maximal WEE1 inactivation rate by MPF. Increasing k_{inactw}

would increasing the rate at which WEE1 concentration drops, leading to longer S/G_2/M phase duration.

- k_{1wee1}
  This parameter is the concentration of MPF at which the WEE1 production is half of its maximal value (given by k_{inactw}). Increasing this parameter would reduce WEE1 degradation rate, leading to longer durations of high WEE1 expression. This would lead to a longer G_1 phase.

- d_{w2}
  This is the degradation term for WEE1. Increasing d_{w2} would lead to increased degradation of WEE1 causing a shorter G_1 phase

2.2.3 Effect of changing the MPF inhibitor parameters

The dynamics of the inhibitor of MPF (z_{10}) are given by Eqn 2.10-

$$\frac{dz_{10}}{dt} = k_{act}(z_8 - z_{10})$$

The dynamics of z_{10} are given simply by its activation by MPF (z_8) and its intrinsic degradation. The only parameter in this eqn is k_{act}, which is the activation rate of the inhibitor of MPF. Increasing the activation rate of the MPF inhibitor would lead to lower MPF expression, which would make all the cell cycle phases shorter.

2.2.4 Appropriate parameters for the four-compartment model

The parameters discussed above need to be altered in a way such that they satisfy the following conditions-

- The concentration of MPF remains low for the longest time during a single cycle. This would ensure a long G_1 phase.

- The rise in MPF should be gradual, such that we can suitably threshold it to define the S and the G_2 phases.

- The fall in the MPF concentration in a single cycle should be rapid. This would lead to a short M phase.

- The thresholds on the MPF concentrations used to define the cell cycle phases should be such that their durations agree with experimental trends (Table 2.1). Furthermore, phase specification by the MPF dynamics should have a biological basis to it.

I perturbed the key parameters that affect cell cycle proteins based on their effects on the cell phase durations. I also set the thresholds that define cell cycle phases based on the MPF oscillation and the desired cell phase duration. I was finally able to set the parameters (Table 2.2) and thresholds (Table 2.3) in such a way that the cell phase durations observed in my simulation closely agree with experimental data (Table 2.4).

Parameter	**Old value**	**New value**
d_{wee1}	5	6
k_{actw}	1	1.24
c_w	1.46	1.29
k_{inactw}	200	175
d_{w2}	1	0.65

Table 2.2: List of changed parameters in the four-compartment model

Phase	**MPF Conc. [nM]**
G_1 to S	>0.033
S to G_2	>0.110
G_2 to M	≤ 0.139
M to cell division	≤ 0.020

Table 2.3: Phase transition thresholds for MPF in the four-compartment model

Phases	**G_1 (hrs)**	**S (hrs)**	**G_2 (hrs)**	**M (hrs)**	**Total time (hrs)**
Expected	11	8	4	1	24
Observed	10.8	7.8	4.2	1.2	24

Table 2.4: Average expected and observed cell cycle phase durations in the four-compartment lineage model.

2.2.5 Adding noise to the model

Similar to the three-compartment model, the dynamics of the molecular species in the four-compartment model are added with Gaussian noise to

simulate their noisy expression. The noise amplitude a_0 in Eqn 2.11 was determined for the four-compartment model by varying it and checking the similarity between the IMT distributions obtained from the simulation and the expected distribution. I observed that noise amplitudes between 0.0008 and 0.0009 lead to IMT distributions that match the expected distribution (Fig 2.4) (Chakrabarti *et al.*, 2018). For all my simulations of the four-compartment model, I have used a noise amplitude of 0.00085.

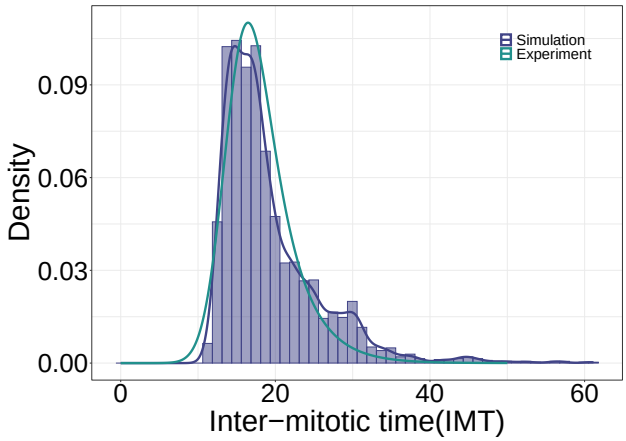

Figure 2.4: Inter-mitotic time distribution obtained from the four-compartment model when a noise of 0.00085 is added. The expected experimental value is taken from Chakrabarti *et al.* (2018)

2.3 Radiation model

The four-compartment model allows us to apply this model to study the effect of radiation on a mixed population of cancerous and normal cells. In order to do this, we need a simulation algorithm that satisfies the following requirements-

- Cells show a drop in the total population post-radiation, depending on the radiation dose
- Cells in different cell cycle phases have different radiosensitivities.
- Cells show cell cycle arrest post-radiation.

In the following sections, I describe the details of these considerations and, finally, lay out the simulation structure I have developed.

2.3.1 Linear-Quadratic model

The Linear-Quadratic (LQ) (Sachs *et al.*, 1997) model is a model that describes the relationship between cell survival post-radiation and the radiation dose. It is given as

$$p(survival) = exp(-\alpha D - \beta D^2) \tag{2.12}$$

where α and β are parameters that describe the radiosensitivity of the cell. These parameters vary with cell type.

The linear quadratic model suggests that the probability of a cell surviving the radiation dose at low doses drops linearly with the dose. However, at higher doses, the probability of cell death drops faster with dosage.

The LQ model does not distinguish between each cell cycle phase. Thus, we need to modify this model in order to predict the fraction of cells surviving post-radiation in a dose and cell-phase-dependent manner.

2.3.2 Phase specific radiosensitivities

Cells in different cell cycle phases show variable radiosensitivities. Cells in the S phase are the least sensitive to radiation-induced DNA damage, while M phase cells have the highest radiosensitivity (Plikus *et al.*, 2013). Chronotherapy aims to manipulate the circadian oscillation in cell phase proportions to target M-phase cells. Thus, our radiation model must include the variable radiosensitivities post-radiation.

In order to model the differential radiosensitivity, I used a modified Linear-Quadratic model similar to the one used by Powathil *et al.* (2013). The new model is as follows -

$$p(survival) = exp(\gamma(-\alpha D - \beta D^2)) \tag{2.13}$$

where α and β are sensitivity parameters as before, and γ is a phase-dependent sensitivity parameter. As the value of γ increases, the radiosensitivity of the phase increases. Thus, we obtain four LQ model equations, one for each cell cycle phase specified by the parameter γ.

The phase-specific sensitivities must be set based on the trend described in Fig 1.5. Thus, the expected trend of the sensitivities is $\gamma_M > \gamma_{G_2} > \gamma_{G_1} > \gamma_S$. In the simulation, $\gamma_{G_1} = 0.3$, $\gamma_S = 0.2$, $\gamma_{G_2} = 0.4$, and $\gamma_M = 1$.

2.3.3 Cell cycle arrest post radiation

Radiation leads to cell cycle arrest in either the G_1 or the G_2 phases, depending on the cell type. Powathil *et al.* (2013) simulated G_1 and G_2 arrest

by randomly sampling an arrest duration for each G_1 and G_2 cell from a uniform random distribution. Each cell is then held in that phase for the sampled duration, after which it can cycle normally.

I only considered G_1 arrest for my simulation, although G_2 arrest can also be added. To simulate cell cycle arrest, I sampled a random arrest time for each cell in the G_1 phase from a normal distribution with a fixed mean and standard deviation. I then arrest the MPF concentration for these cells for the duration sampled for that cell. Following that, the cell is allowed to cycle normally. The mean and variance of the G_1 arrest were obtained from the data by Reyes *et al.* (2018).

2.3.4 Radiation model overview

Having taken into account the considerations mentioned above, I developed a radiation model simulation using the simulation for the four-compartment model. Similar to the four-compartment model, we can specify the autonomous cell cycle period and the strength of the clock-cell cycle coupling. Furthermore, one needs to input the parameters for the LQ model (α and β). I used experimentally obtained values of these parameters for HCT116 cells (Miller *et al.*, 1992) and set α to 0.479 and β to 0.067. Furthermore, one needs to specify the phase-specific sensitivities (γ_i) for each cell cycle phase i. Using α, β, and γ_i, we can obtain the phase-specific cell survival probabilities denoted as p_{G_1}, p_S, p_{G_2}, and p_M using Eqn 2.13. We also need to specify the irradiation time and the radiation dosage. Lastly, we need to specify the mean and the variance of the G_1 arrest post-irradiation. The release time in the simulation was sampled from a normal distribution with a mean of 18 hours and a standard deviation of 4 hours based on experiment data on HCT116 cells.

Using these input parameters, the simulation generates cell lineages that proliferate normally before radiation. At the time of radiation, a random number is uniformly sampled between 0 and 1 for each cell. The sampled values are then compared with the survival probabilities depending on the phase of the individual cells. The irradiated cells with a sampled value lower than the survival probability of their phases survive, and the rest are killed.

After radiation, cells that are in the G_1 phase are assigned a release time by randomly sampling values from a normal distribution with the mean and variance specified by the inputs. The MPF concentration of these cells is not updated as per Eqn 2.8, but they are held constantly to the concentration just before irradiation. Cells in the S, G_2 and M phases are allowed to divide normally once, after which the daughter cells undergo G_1 arrest. After a cell completes its arrest duration, its molecular concentrations are updated

normally.

2.4 Kuramoto model

The circadian clock-cell cycle network is a complicated network that can be simplified by considering them as two coupled oscillators, each oscillating with its intrinsic frequency. Oscillators are said to be synchronized when they oscillate with the same frequency ω. When oscillators with different intrinsic oscillation frequencies are coupled to each other, their frequency gets altered by varying degrees, and they synchronize over time depending on the strength of the coupling.

The coupled oscillator model was originally studied by Winfree in 1967 (Winfree, 1967), who studied identical oscillators that are weakly coupled to each other. He used a mean-field approach wherein he assumed that all oscillators are coupled to the average rhythm generated by the entire population.

$$\dot{\theta}_i = \omega_i + (\sum_{j=1}^{n} X(\theta_j)Z(\theta_i)$$

where θ_i is the phase of the i^{th} oscillator, ω_i is its angular velocity. Each oscillator j exerts its effect, $X(\theta_j)$ on the oscillator i through $Z(\theta_i)$. Strogatz (2000) gives a brief history of the Kuramoto model and describes how Winfree's work inspired Kuramoto.

Kuramoto (1984) used a reductive perturbation method, where he considered very weakly perturbed oscillators near the Hopf bifurcation point. Kuramoto considered the simplest case of identical oscillators coupled equally to each other by a sinusoidal coupling.

Say we have N identical oscillators, each with an intrinsic angular velocity ω_i. These angular velocities are distributed according to some unimodal and symmetric distribution function $g(\omega)$. Suppose that the oscillators are globally coupled to each other by a coupling factor K. Then, the Kuramoto model states that the angular velocity of each oscillator is

$$\dot{\theta}_i = \omega_i + \frac{K}{N}\sum_{j=1}^{N} sin(\theta_j - \theta_i) \tag{2.14}$$

In the following sections, I describe the behavior of the Kuramoto model, its simplification, and its application to the clock-cell cycle system.

2.4.1 Model Analysis

The first term in Eqn 2.14 is the intrinsic angular velocity of the oscillator. In the absence of any coupling, we would expect each oscillator to oscillate with this angular velocity. The second term affects the angular velocity of each oscillator based on its coupling to the other oscillators. For any other oscillator with phase θ_j, the following three cases arise:

1. $\theta_i < \theta_j$
   This means the i^{th} oscillator is phase lagging to the j^{th} oscillator. In this case, $sin(\theta_j - \theta_i)$ is positive. This term contributes to speeding up the angular velocity of the i^{th} oscillator. Note that in the expression for the angular velocity of the j^{th} oscillator, there will be a term $sin(\theta_i - \theta_j)$. This term would be negative, implying that it contributes to slowing down the j^{th} oscillator. Thus, we see that the coupling function acts on the phase-lagging oscillator to speed it up while simultaneously acting on the phase-advanced oscillator to slow it down.

2. $\theta_i = \theta_j$
   This means that both oscillators are in the same phase. This implies that the $sin(\theta_j - \theta_i)$ term is zero. Thus, synchronized oscillators do not affect each other's angular velocity.

3. $\theta_i > \theta_j$
   This case is the opposite of the first one. Here, $sin(\theta_j - \theta_i)$ is negative leading to the i^{th} oscillator to slow down, while the j^{th} oscillator to speed up.

Thus, in a system of N oscillators, we expect the oscillators with a higher angular velocity to slow down while the ones with a lower angular velocity speed up.

2.4.2 Order parameter

Kuramoto further simplified his model by looking at mean-field dynamics by defining the order parameter as -

$$R(t)e^{i\Theta(t)} = \frac{1}{N}\sum_{j=1}^{N} e^{i\theta_j(t)} \tag{2.15}$$

Here $R(t)$ gives the level of coherence between the oscillators. $R(t) = 0$ implies perfect non-coherence, implying that the oscillators are not synchronized at all. $R = 1$ implies perfect synchrony of the oscillators. The order parameter is essentially the average of the positions of all the oscillators.

We can write 2.14 in terms of the order parameter as follows

$$\begin{aligned}\dot{\theta_i} &= \omega_i + K\mathfrak{Im}(\frac{1}{N}\sum_{j=1}^{N} e^{i(\theta_j-\theta_i)}) \\ &= \omega_i + K\mathfrak{Im}(\frac{e^{-i\theta_i}}{N}\sum_{j=1}^{N} e^{i\theta_j}) \\ &= \omega_i + K\mathfrak{Im}(R(t)e^{i\Theta(t)}e^{-i\theta_i}) \\ \dot{\theta_i} &= \omega_i + KRsin(\Theta-\theta_i) \end{aligned} \tag{2.16}$$

The order parameter summarizes the behavior of the oscillators, making it convenient to study. Kuramoto found that a system of oscillators shifts from being asynchronous to synchronous at a critical coupling value, K_c. Synchronization occurs when the oscillators oscillate with the same angular velocity. If all oscillators oscillate with the same constant angular velocity, we say that the system is fully synchronized. If $n < N$ oscillators oscillate with a constant angular velocity, then the system is said to be partially synchronized. Kuramoto found that for a coupling value $K < K_c$, the system cannot be synchronized. The system can be synchronized partially or fully for $K > K_c$. The synchronization increases as K increases and complete synchrony is achieved at some coupling value. The value of K_c is dependent on $g(\omega)$.

2.4.3 Application of the Kuramoto model to study clock-cell cycle dynamics

The clock and the cell cycle can be modeled as coupled oscillators with individual intrinsic time periods. Determining the phase of entrainment for the clock-cell cycle system is important to understand the feasibility of chronomodulated radiation strategies in cancer therapy. We can do this using the Kuramoto model for a pair of oscillators.

The Kuramoto model for a pair of coupled oscillators

Consider two oscillators, O_1 and O_2, that are coupled to each other in a sinusoidal manner with a constant coupling factor K. We can write 2.14 for these two oscillators as,

$$\dot{\theta_1} = \omega_1 + \frac{K}{2}sin(\theta_2-\theta_1)$$
$$\dot{\theta_2} = \omega_2 + \frac{K}{2}sin(\theta_1-\theta_2)$$

We can solve these equations,

$$\dot{\theta_2} - \dot{\theta_1} = \omega_2 - \omega_1 + \frac{K}{2} sin(\theta_1 - \theta_2) - \frac{K}{2} sin(\theta_2 - \theta_1)$$
$$\dot{\theta_2} - \dot{\theta_1} = \omega_2 - \omega_1 - K sin(\theta_2 - \theta_1)$$

Let $\phi = \theta_2 - \theta_1$. Thus ϕ is the phase difference between the oscillators. The time derivative of ϕ, $\dot{\phi} = \dot{\theta_2} - \dot{\theta_1}$, if the difference in the angular velocities of O_2 and O_1. Let Ω be the difference in the intrinsic angular frequencies of the oscillators, $\Omega = \omega_2 - \omega_1$. Substituting these, we obtain

$$\dot{\phi} = \Omega - K sin(\phi) \tag{2.17}$$

At steady state, $\dot{\phi} = 0$. From 2.17, we have

$$\hat{\phi} = sin^{-1}(\frac{\Omega}{K}) \tag{2.18}$$

where $\hat{\phi}$ is the steady state phase of entrainment.

Using this model, we can study the steady-state dynamics of the clock and cell cycle for cancer and normal cells. Comparing the phases of entertainment of these cells would tell us the phase difference in the cell cycles between these cell types, thus allowing us to predict the therapeutic window.

One drawback of this approach is the assumption of the sinusoidal coupling between the clock and the cell cycle. The nature of the coupling between the clock and the cell cycle is poorly understood. While estimates of the coupling value can be obtained (Droin *et al.*, 2019), the sinusoidal response of the cell cycle to the circadian clock has not been noted before. This requires us to consider a more general description of the Kuramoto model. A general formulation of the Kuramoto model can be stated as follows

$$\frac{d\theta_i}{dt} = \Omega + \sum_{j=1}^{N} \Gamma_{ij}(\theta_j - \theta_i) \tag{2.19}$$

where Γ_{ij} is the influence of the j^{th} oscillator on the i^{th} oscillator. For very weak coupling between identical oscillators, we can consider Γ_{ij} to be the convolution of two functions

$$\Gamma_{ij}(\phi) = \frac{1}{2\pi} \int_0^{2\pi} p_j(t) Z_i(t - \phi) dt \tag{2.20}$$

where ϕ is the phase difference between the i^{th} and the j^{th} oscillators, $p_j(t)$ is the perturbation applied by the j^{th} oscillator and $Z_i(\phi)$ is the Phase Response

Curve (PRC) of the perturbed oscillator. The PRC is the response of a perturbed oscillator to infinitesimal perturbations as a function of the phase at which the perturbation arrives. Note that averaging the perturbation over a complete cycle can only be done for weakly coupled oscillators (Breakspear *et al.*, 2010).

Granada *et al.* (2013) consider Eqn 2.19 along with Eqn 2.20 for a pair of oscillators and state the Kuramoto model as

$$\frac{d\phi}{dt} = \Omega + K \int_0^{2\pi} p(t)Z(t-\phi)dt \tag{2.21}$$

where $\phi = \theta_2 - \theta_1$ is the phase difference between the oscillators, Ω is the angular velocity difference, K is the coupling constant, and the other variables are as in Eqn 2.20.

To study the steady-state dynamics of the clock-cell cycle coupled oscillator system, we need an understanding of the PRC of the cell cycle in response to the clock. If the coupling between these two oscillators can be modeled using a sinusoidal function, then we will be able to easily predict the phase difference between the circadian clock and the cell cycle oscillator at a steady state (Eqn 2.18). However, generating a PRC for the cell cycle oscillator is not straightforward since the clock cannot discretely and infinitesimally perturb the cell cycle. To address this problem, I looked for methods that could infer the Phase Response Curve of a continuously perturbed oscillator. This led me to an iterative algorithm given by Cestnik and Rosenblum (2018), which infers a finite Fourier approximation of the PRC using an iterative algorithm.

2.5 Inferring the PRC of the cell cycle oscillator

The Phase Response Curve (PRC) is the phase shift of an oscillator to an infinitesimal perturbation that arrives at a particular phase of the oscillator. The PRC of an oscillator is typically constructed by perturbing an oscillator infinitesimally and then calculating its net phase shift over subsequent cycles, i.e., if the autonomous period of the oscillator is T_0, and a perturbation of magnitude ϵ is applied to it then the PRC is given as

$$Z(\phi) = 2\pi \frac{nT_0 - \sum_{i=1}^{n} T_i}{\epsilon T_0} \tag{2.22}$$

where $\{T_i\}_{i=1}^{n}$ are the periods of the oscillator post the perturbation, and n is chosen sufficiently large so that the oscillator settles back to its limit cycle.

For the clock-cell cycle coupled oscillator system, the discrete perturbation method of obtaining the PRC is challenging. We cannot discretely perturb the cell cycle by the clock. Hence, we turn to a method given by Cestnik and Rosenblum (2018) that can help us estimate the PRC of a continuously perturbed oscillator.

A continuously perturbed oscillator can be modeled by the phase model as follows

$$\dot{\phi} = \omega + Z(\phi)p(t) \tag{2.23}$$

where ϕ is the instantaneous phase of the oscillator, ω is its intrinsic angular velocity, $Z(\phi)$ is the PRC of the oscillator and $p(t)$ is the input perturbation. Cestnik and Rosenblum (2018) considered a finite Fourier transformation of $Z(\phi)$.

$$Z(\phi) = a_0 + \sum_{n=1}^{N}[a_n cos(n\phi) + b_n sin(n\phi)] \tag{2.24}$$

Substituting Eqn 2.24 in Eqn 2.23 and integrating over a complete cycle we get

$$\begin{aligned} 2\pi =& \omega T_m + a_0 \int_{t_m}^{t_m+T_m} p(t)dt + \sum_{n=1}^{N}[a_n \int_{t_m}^{t_m+T_m} p(t)cos[n\phi(t)] \\ &+ b_n \int_{t_m}^{t_m+T_m} p(t)sin[n\phi(t)]] \end{aligned} \tag{2.25}$$

where $[t_m, t_{m+1}]$ is a time interval over which the phase of the oscillator varies from 0 to 2π, and $T_m = t_{m+1} - t_m$. Identifying the inter-event interval, $[t_m, t_{m+1}]$, is not a trivial task and can be done using a Poincare section of the limit cycle of the oscillator.

The algorithm given by Cestnik and Rosenblum (2018) begins with a linear approximation of the phase, $\phi^{(0)}(t) = 2\pi\frac{(t-t_m)}{T_m}$. It then uses an iterative method to obtain the PRC as follows -

1. Identify the inter-event intervals, $[t_m, t_{m+1}]$

2. Plug in the phase estimate $\phi^{(k)}(t)$ in Eqn 2.25 for each inter-event interval

3. Obtain the coefficients in Eqn 2.25 using a linear fit. This gives us estimates of the angular velocity $\omega^{(k+1)}$ and $Z^{(k+1)(\phi)}$

4. Plug $\omega^{(k+1)}$ and $Z^{(k+1)(\phi)}$ in Eqn 2.23 and numerically integrate to obtain a new estimate of the phase $\phi^{(k+1)}(t)$

5. Since $Z^{(k+1)(\phi)}$ is only an estimate of the PRC, the phase function can be such that $\phi^{(k+1)}(t_m + T_m) = \psi_m^{(k+1)}$, where $\psi_m \neq 2\pi$. Thus, we rescale the phase as $\phi^{(k+1)}(t) \rightarrow 2\pi \frac{\phi^{(k+1)}(t)}{\psi_m^{(k+1)}}$

A rather helpful part of this model is the ease of error estimation. For model validation, we began by using known PRCs ($Z^{(t)}(\phi)$). In such cases, the error of estimation is given by

$$\Delta_Z = \frac{||Z^{(t)} - Z^{(r)}||}{||Z^{(t)}||} \tag{2.26}$$

In general, the true PRC is not known. In such a situation, this model suggests a straightforward error estimation method. We expect the reconstructed phase to be 2π at the end of each interval in step 4 above. Thus, a simple error estimate is the deviation of the reconstructed phase at the end of each interval from 2π

$$\Delta_\psi = \langle(\psi_m - 2\pi)^2\rangle^{\frac{1}{2}} \tag{2.27}$$

Δ_ψ can be obtained directly from the data. One issue with this error estimate is that it also depends on the irregularity in the inter-event intervals. Hence, Cestnik and Rosenblum (2018) propose an inter-event irregularity error estimate -

$$\Delta_{\psi_T} = \langle(\langle\omega\rangle T_m - 2\pi)^2\rangle^{\frac{1}{2}} \tag{2.28}$$

where $\langle\omega\rangle$ is the average angular velocity of the oscillator.

The error in the PRC reconstruction is low if $\Delta_\psi << \Delta_{\psi_T}$. This would mean that the iterative algorithm reconstructs a PRC and angular velocity that can explain the data much better than a perfectly periodic oscillator with an angular velocity $\langle\omega\rangle$.

I wrote a code in R for this algorithm. I also compared my results with the code available online by Cestnik. To test my code, I tried to replicate Figure 1(b) in Cestnik and Rosenblum (2018). They use a known PRC given by

$$Z(\phi) = (1 - cos(\phi))exp(3[cos(\phi - \frac{\pi}{3}) - 1]) \tag{2.29}$$

They generate spike data by using an autonomous angular velocity (ω) 1 and using the Ornstein-Uhlenbeck process as an input perturbation (Eqn 2.30).

$$\dot{p} = -\frac{p}{\tau} + \epsilon\sqrt{\frac{2}{\tau}}\xi(t) \tag{2.30}$$

where ξ is Gaussian noise and ϵ and τ are the amplitude and the correlation time of the perturbation respectively.

I ran the PRC reconstruction algorithm on the phase oscillation data that resulted from Eqn 2.23 using Eqns 2.29 and 2.30. I also used the online available code to reconstruct the PRC.

Chapter 3

Experimental Methods

3.1 Cell culture

HCT116 cells (ATCC CCL-247) were borrowed from Dr Sabrinathan Radhakrishnan. The cells were cultured in McCoy's 5A Medium (Gibco Cat No-16600082) supplemented with 10% Fetal Bovine Serum (FBS) and 1% PenStrep. They were frozen down using a freezing mix given in Table 3.1. The freeze-downs were first maintained at -80^o C and then transferred to a liquid Nitrogen tank.

Component	**Concentration**
Fetal Bovine Serum (FBS)	90%
DMSO	10%

Table 3.1: Freezing mixture composition

For thawing a vial, we place the frozen vials in a water bath at 37^o C. The DMSO is quenched with pre-warmed fresh complete medium and centrifuged at 1500 rpm for 5 mins. The supernatant is aspirated, and the pellet is resuspended in 1 mL complete medium. The cells are then transferred to a T25 flask containing 2 mL complete medium.

HCT116 cells were passaged using 0.05% Trypsin. The detached cells were flushed with a complete medium and centrifuged at 1500 rpm for 5 mins. The supernatant was aspirated, and the cell pellet was resuspended in fresh complete medium. If a specific cell number is to be seeded for an experiment, we count the number of cells per mL using Countess^{TM} 3 Automated Cell Counter (Cat no.: AMQAX2000) and make a cell dilution as per the requirements. We then transfer the cells to an appropriate culture medium.

3.2 Cell cycle staining using DAPI intensity

HCT116 cells were seeded in 35mm punched dishes with 1.5mm coverslips. After an initial incubation period to allow the cells to attach, we synchronized half the plates using 1mL of 100nM Dexamethasone. These plates were incubated for an hour, after which the Dexamethasone-containing medium was replaced with fresh complete medium. Following that, plates were fixed at 4hr intervals using 4% Paraformaldehyde for 15 mins. After 15 mins, the PFA was aspirated, and the cells were given a 1x PBS wash. The dishes were stored in 4°C until DAPI staining.

For DAPI staining, the dishes were given a 1x PBS wash for 2 mins, following which 0.5% Triton-X solution was added. After a 15 min incubation at room temperature, the dishes were given a 1x PBS wash for 2 mins. 0.1μg/mL DAPI solution was added to the dishes. After 3 mins, the DAPI solution was aspirated, and the cells were washed with 1x PBS. High salt mounting medium was added to the dishes, after which they were imaged.

3.3 Imaging

The DAPI-stained cells were imaged using a 60X oil objective in a Nikon Ti2e inverted microscope. For each field of view, Z-stacks were set such that the nuclei were not extremely out of focus in any stack. In our first round of imaging, we observed that the nuclear fluorescence was too high, and the camera sensor was saturated (Fig 4.17). This resulted in inaccurate cell phase proportion predictions. In subsequent imaging, we lowered the input LED intensity, thus ensuring the nuclear fluorescence did not exceed the dynamic range of the DAPI channel.

3.4 Image analysis

Image analysis was done using the cellpose package in Python and ImageJ. The raw DAPI images were first denoised using the BaSic plugin in ImageJ. The flat field corrected images were average projected. These images were then imported into the cellpose GUI, where a nuclear segmentation model was trained. The trained model was used to segment all the nuclei which gave the nuclear masks. These masks were then overlayed on the flat field corrected DAPI images using the MorphoLibJ plugin in ImageJ. This gave the mean intensity of each cell and its area. These two quantities were multiplied to obtain the total nuclear DAPI intensity for each cell.

To obtain the cell cycle phase proportions for each time point, the total DAPI intensities were obtained from cells fixed at different time points. The total intensity was rescaled by a suitable power of 10 to make the intensity a single digit. This prevents computational overflow. The rescaled intensity values were fit to a mixture model involving a mixture of two univariate normal distributions (Eqn 3.1).

$$I \sim a\mathcal{N}(\mu_1, \sigma_1) + (1-a)\mathcal{N}(\mu_2, \sigma_2) \tag{3.1}$$

The fitting was done using the `flexmix` package in R. The weight corresponding to the Normal distribution with the lower mean gives the fraction of cells in the G_1 phase. If a single normal distribution fits the total intensity profile, the G_1 proportion depends on the mean of the distribution. If the mean is lower than 1.7, the G_1 proportion is set to 1 else, it is set to 0. The cutoff for the mean intensity comes from Dhuppar and Mazumder (2018), who used a mixture model to fit their data using the condition that the mean of the G_2 peak is 1.7 - 2.3 times the mean of the G_1 peak.

Rhythmicity analysis for the G_1 proportion was done using a package called `ODeGP` (Sahay *et al.*, 2023), which combines Gaussian Process (GP) regression with Bayesian inference to detect rhythmicity in noisy datasets. This model requires time series data as an input and outputs the strongest detected period of oscillation in the data. It also compares the oscillatory model with a no-oscillation model to give a Bayes factor which is used to determine if the data is oscillatory or not. The threshold on the Bayes factor is 14.

3.5 Flow Cytometry

HCT116 cells were seeded in 26 35mm cell culture dishes and grown for 48 hours. After 48 hours, 13 plates were synchronized using 100nM Dexamethasone in complete medium, while 13 were left unsynchronized. After adding Dexamethasone, the cells were incubated at 37°C for 1 hr. Following that, a medium change was given to all plates, and two plates were fixed, one synchronized and the other unsynchronized.

For fixing the cells, the existing medium was aspirated and the 35 mm dish was given a 1x PBS wash. After the wash, 500 μL 0.05% Trypsin was added to the dish, and the cells were incubated at 37°C for 3.5 mins. After the incubation, the Trypsin was quenched with 2mL complete McCoy's 5A medium. The dish was flushed to ensure that all cells had detached, after which the cell suspension was transferred to a 15 mL centrifuge tube. The cells were spun at 1500 rpm for 5 mins. The supernatant was discarded,

and the cell pellet was resuspended in 1 mL of an RNAase buffer (1mg/mL Trisodium Citrate, 40μg/mL RNase, and 0.03% IGEPAL CA-360 in ddH_2O). The cell suspension was vortexed and left for 5 mins at room temperature. Then, 2mL of chilled 100% ethanol was added to the tube, and the cells were stored at 4°C. This procedure was repeated every four hours for a synchronized and unsynchronized culture, leading to 13 time points across 48 hrs.

For staining the cells with PI, the cells were centrifuged at 1500 rpm for 5 mins, and the supernatant was aspirated. The cell pellet was suspended in PI solution and incubated for 10 mins. The cells were then imaged in a

Chapter 4

Results

4.1 Three-compartment model

We developed a lineage-generating simulation using the circadian clock-cell cycle model proposed by El Cheikh *et al.* (2014). This model can simulate the molecular dynamics of the clock and cell cycle genes (Fig 4.1) and use these dynamics to simulate cell division. The simulation starts with an input of N identical cells with pre-specified molecular concentrations. Three key parameters need to be specified in the simulation-

- The noise amplitude, a_0
- The clock-cell cycle coupling constant, C
- The average autonomous cell cycle period of the cells, τ

The simulation then uses Eqns 2.1-2.10 with additive Gaussian noise to update the molecular concentrations of each cell and uses MPF thresholds to simulate the cell cycle.

In the absence of noise, we have a fully deterministic system, which is easier to study. I used noise-free simulations to validate the oscillation of the clock and cell cycle components in the simulation to see if our simulation agreed with the results from El Cheikh *et al.* (2014). I initialized my simulation with a single cell in the G_1 phase with set molecular concentrations. I ran my simulation with a_0 and C set to 0. The autonomous period of the cell (τ) is set to 18 hrs. As shown in Fig 4.1, the BMAL1, PER2, WEE1, and MPF concentration graphs show sustained oscillations even in the absence of coupling. These results agree with El Cheikh *et al.* (2014)'s findings, confirming that our molecular concentrations are being updated correctly. When clock coupling is added ($C = 0.5$), the period of the MPF oscillation

gets entrained to that of the clock (Fig 4.2). These results hold even after noise (with a noise amplitude of 0.0025) is incorporated into the model (Fig 4.3). Henceforth, all the results presented have noise incorporated in the ODEs, leading to a stochastic gene expression profile.

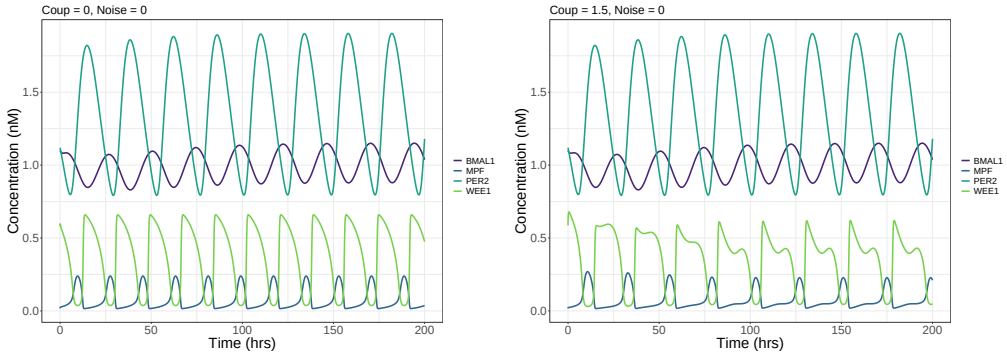

Figure 4.1: Clock and cell cycle gene expression in the three-compartment model without noise. On the left, the clock is not coupled to the cell cycle, while on the right, the clock coupling is 1.5.

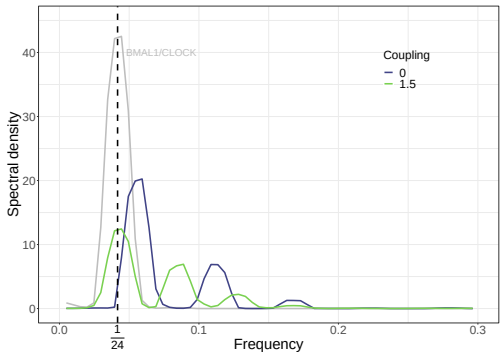

Figure 4.2: Spectral analysis of MPF oscillations in the clock coupled and uncoupled system shows that the cell cycle gets entrained to the period of the clock when coupled to it.

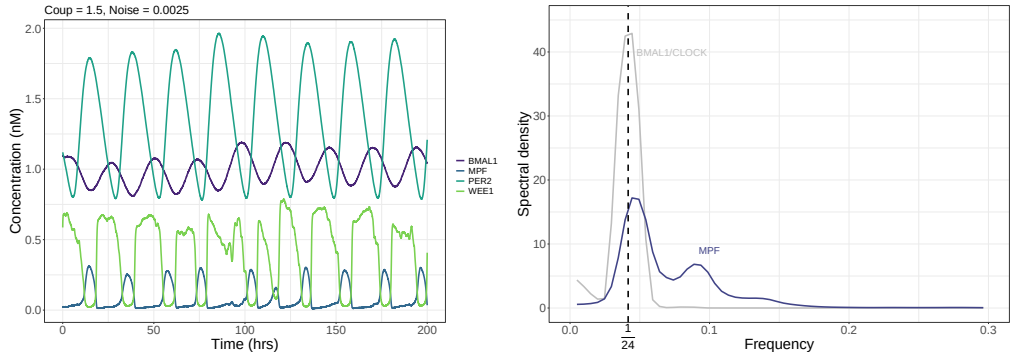

Figure 4.3: When noise is added to the three-compartment model, we obtain clock and cell cycle oscillations (left) and entrainment of the cell cycle by the clock (right). The coupling constant was set to 1.5.

For simulations that start from a single cell, the fraction of cells in a particular phase shows oscillatory patterns only when the clock is coupled to the cell cycle (Fig 4.4). This behavior can be explained by the entertainment of the period of MPF to that of the clock on coupling the two. This is also reflected in the period of the phase proportion oscillations. Despite the autonomous cell cycle time being 18 hrs, the fraction of cells in each cell cycle phase oscillates with a period of 24 hrs (Fig 4.5). In the absence of coupling, we see an initial transient oscillation pattern. The initial step-like oscillatory behavior is observed since we started our simulation from a single cell, leading to 100% synchrony in the cells at the start.

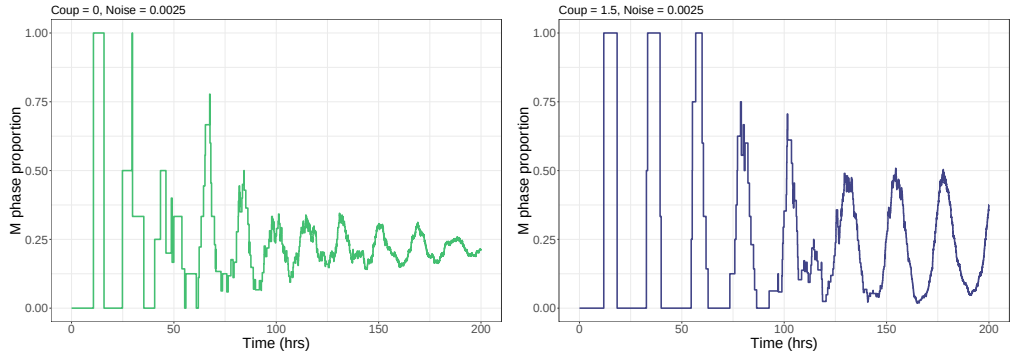

Figure 4.4: Clock and cell cycle gene expression in the three-compartment model shows sustained oscillations when the clock is coupled to the cell cycle. On the left, the clock coupling is 0, while on the right, the clock coupling is 1.5.

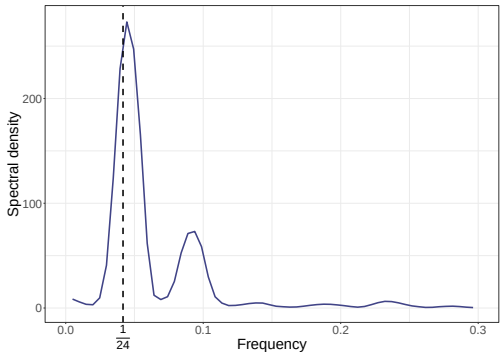

Figure 4.5: Spectral analysis of the M phase proportion in the clock coupled system shows that it oscillates with a dominant period of 24 hours.

We can start our simulation from any arbitrary number of cells, each with a different initial molecular concentration. Starting from a single cell is equivalent to starting from N identical cells. These cells have identical molecular concentrations and belong to the same cell cycle phase at the start of the simulation. I ran a simulation starting with 50 identical cells in the G_1 phase for 200 simulation time. As shown in Fig 4.6, in the absence of coupling, the fraction of cells in each cell cycle phase oscillates initially, after which it settles to a constant value. The initial oscillations are observed because we start the simulation with identical cells that are in the same cell cycle phase. These cells cycle through the cell cycle together. However, noise makes each cell's duration in a particular phase variable, leading to the desynchronization of cells over time. Thus, the cell phase proportions reach a constant value.

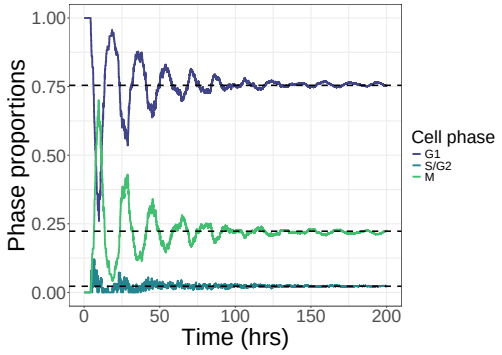

Figure 4.6: Proportion of cells in each cell cycle phase when we start the simulation with 50 identical cells in the G_1 phase in the absence of clock coupling. The dotted lines are the expected cell cycle phase proportions at steady state obtained from Eqn 4.1

The fraction of cells in each cell cycle phase, in the absence of external perturbation by the clock, can be predicted by the ergodic theory. The ergodic principle states that the fraction of cells in a particular cell cycle phase is proportional to the duration of that phase. Wheeler (2015) applied the ergodic principle to study the fraction of cells in each cell cycle phase. Since a cell division event leads to the death of a single cell but its replacement by two daughter cells, the fraction of cells in the G_1 phase is higher than what is predicted by simple ergodicity. Correcting for this, Wheeler described the fraction of cells including and up to a phase n, $p_{\leq n}$ as -

$$p_{\leq n} = 2(1 - 2^{-t_{\leq n}/T}) \tag{4.1}$$

where $t_{\leq n}$ denotes the duration of phases up to and including phase n. This rule applies only in cases where the cell cycle does not have any external perturbations by the clock. If the fraction of cells in each cell cycle phase obtained from our simulation data with no clock coupling matches that predicted by Eqn 4.1, then the lineage generated by our simulation follows the ergodic principle, validating the simulation.

I obtained the mean cell phase durations and the mean cell cycle time for the data shown in Fig 4.6. Using Eqn 4.1, I calculated the expected proportion of cells in each cell cycle phase at steady state. As shown in Fig 4.6, the fraction of cells in each cell cycle phase settles to the value predicted by Eqn 4.1. This validates the lineage generation in our model.

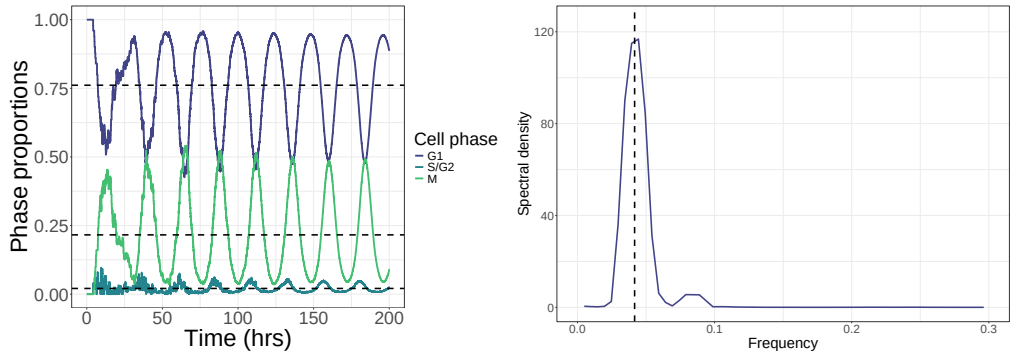

Figure 4.7: Proportion of cells in each cell cycle phase when we start the simulation with 50 identical cells in the G_1 phase in the presence of clock coupling (left). The dotted lines are the expected phase proportions obtained from Eqn 4.1. Spectral analysis of the M phase proportion in the clock-coupled system shows that it oscillates with a dominant period of 24 hours (right).

When the clock is coupled to the cell cycle, we observe that the fraction of cells in each cell cycle phase shows a sustained oscillation (Fig 4.7). The

period of this oscillation matches that of the clock (Fig 4.7). Such circadian oscillation in clock-controlled proliferating cells has been observed experimentally by Plikus *et al.* (2013) in mouse hair cortical cells. Thus, our model is able to replicate the oscillatory behavior in proliferation that is observed experimentally.

In a real-life setting, we do not expect the cells to be phase-synchronized at the start. In order to model this, we generated a starting population of 50 cells with varying clock and cell cycle expression by sampling them from the end of a previously run simulation. These cells can be used to simulate a starting population of asynchronous cells under the same clock control but at varying stages of the cell cycle.

Using the asynchronous starting population, I ran a simulation to study the phase proportion oscillations. In the absence of clock coupling, the fraction of cells in each cell cycle phase settles to a constant value, as predicted by Eqn 4.1 (Fig 4.8). The initial oscillations observed in the synchronized initial population are no longer observed. When clock coupling is added, the fraction of cells in each cell cycle phase oscillates around a mean predicted by Eqn 4.1 (Fig 4.8). As the coupling strength is increased, the amplitude of these oscillations increases, suggesting that more cells are synchronized (Fig 4.9). An interesting behavior that we observe is that the phase proportion oscillations show 24-hour oscillations regardless of the coupling strength (Fig 4.9).

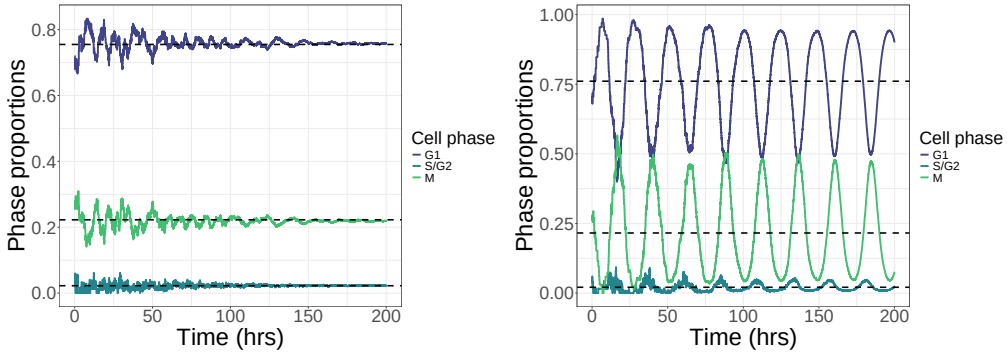

Figure 4.8: Proportion of cells in each cell cycle phase settles to the expected value predicted by Eqn 4.1 (shown by the dotted line) in the absence of clock coupling(left). In the presence of clock coupling, the phase proportions oscillate with a mean given by Eqn 4.1. The simulations were started with an asynchronous starting population.

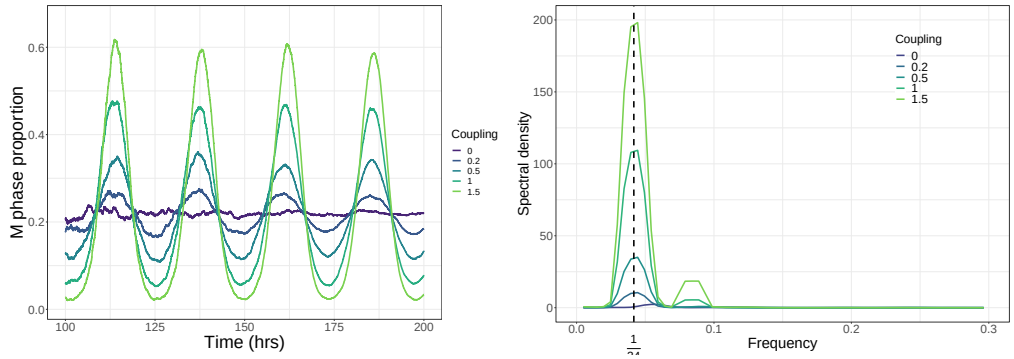

Figure 4.9: Proportion of cells in the M phase shows an increase in synchrony with an increase in coupling(left). The dominant period of oscillation is 24 hours, regardless of coupling (right).

To test how cancer and normal cell cycle dynamics vary in a clock-coupled system, I used the three-compartment model to simulate cell cycle dynamics of clock-coupled cells having autonomous cell cycle periods (τ) 18, 20, 25, and 26. The coupling between the clock and the cell cycle was identical for all the cell types. While the fraction of cells in the M phase oscillates with a circadian period, we see peaks in the oscillation patterns at different times for the different cell types (Fig 4.10). The cells with an autonomous period of 26 hours show a phase delay of 5.6 hours in the M phase proportion oscillations compared to the cells that cycle at 18 hours. As the autonomous cell cycle period rises, the M phase proportion oscillations show a phase delay in their oscillation pattern. We also notice an increase in the amplitude of the M phase proportion oscillation with the autonomous period. This is due to an increase in synchronicity in cells that intrinsically cycle with a period close to the period of the circadian clock.

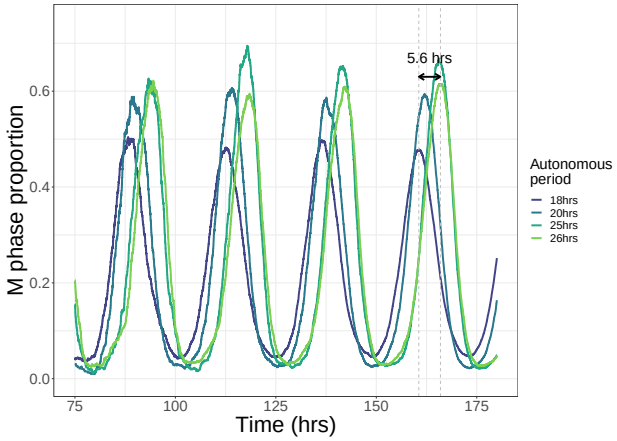

Figure 4.10: M phase proportion oscillations for cells having different autonomous periods. As the autonomous period increases, the M phase peak comes at a later time.

4.2 Four-compartment model

The radio-resistance of the S and G_2 phase is quite different. Thus our three-compartment model is not directly applicable to model the effects of radiation on cells. I developed a four-compartment model by varying different model parameters. This model uses the same molecular dynamics equations as the ones in the three-compartment model but is able to classify cells into the G_1, S, G_2, and M phases.

The cell cycle phase durations obtained for each cell in the four-compartment model follow the expected trend (Fig 4.11), with G_1 being the longest phase and the S phase being the shortest. We further see that the means of the G_1, S, G_2 and M phases are 10.8 hrs, 7.8 hrs, 4.2 hrs, and 1.2 hrs, respectively. These values have also been observed experimentally for 24-hour cycling human cells (Cooper, 2000).

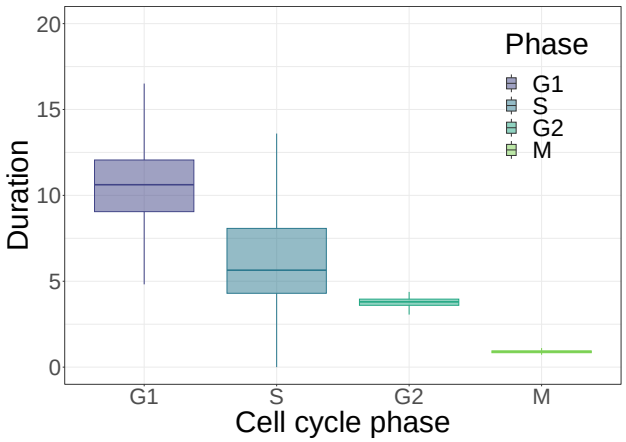

Figure 4.11: The duration of each phase of the cell cycle obtained from the simulation follows the trend that we expect from normal human cells.

Using this model, I began by studying the behavior of phase proportion oscillations under different values of coupling. In the following sections, I describe some key findings from this model.

4.2.1 Phase population proportions oscillate with clock coupling

I ran the four-compartment model starting from a single cell with an autonomous cell cycle period of 18 hrs for different coupling values (0, 0.25, 0.5, and 1) and plotted the cell fraction in each phase over time. A representative graph of the fraction of cells in the S phase is shown in Fig 4.12. In the absence of coupling between the clock and the cell cycle, the fraction of cells in the S phase oscillates initially. However, these oscillations die over time, and the S phase proportion settles to a constant value. As the coupling parameter increases, the amplitude of the oscillation of the proportion of cells in the S phase rises, indicating that more cells are simultaneously in the same cell cycle phase.

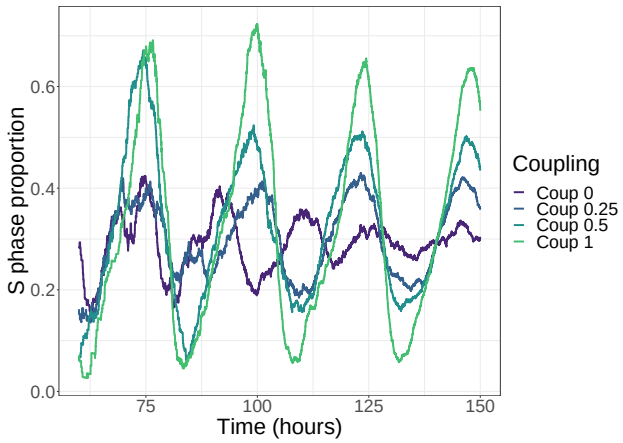

Figure 4.12: The fraction of cells in the S phase oscillates when the clock is coupled to the cell cycle. Furthermore, the synchronicity of the cells increases with higher clock coupling.

4.2.2 Phase population proportions oscillate with the same period

Similar to the three-compartment model, coupling the clock to the cell cycle leads to nearly 24-hour oscillations of the S phase proportions despite the autonomous cell cycle period (the cell cycle period in the absence of clock coupling) being 18 hours (Fig 4.13). The period of these oscillations does not depend on the coupling constant.

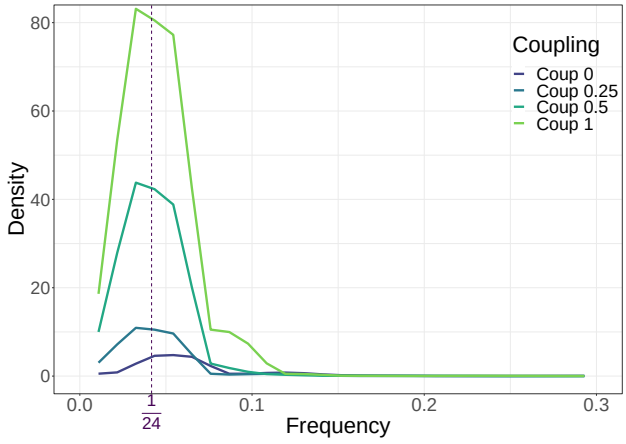

Figure 4.13: Fourier transform of the S phase proportion oscillations seen in Fig 4.12. The dotted line represents a period of 24 hours.

4.2.3 Difference in division times opens a therapeutic window

The influence of the circadian clock on the period of phase proportion oscillations (Fig 4.12) raises questions about the entrainment of a mixed population of cancer and normal cells since these have different intrinsic cycling periods. If both cell types are coupled to the clock, we expect them to progress through the cell cycle with the same period, albeit a phase shift in the times when most cells are in a particular phase.

I ran a simulation with constant coupling and varying cell cycle times to study the behavior of clock-controlled cancer and normal cells. I chose fast-cycling cells with a division time of 12, 18, and 20 hours and slightly slower-cycling cells with a mean division time of 25 hours. We observe that the time when most cells are in the S phase differs for each cell type (Fig 4.14). As the autonomous cycling period of the cells increases, the peak of the relative S phase population shifts further right. The S phase peak for cells that cycle with a period of 25 hours comes 8 hours after that of cells cycling with a period of 18 hours.

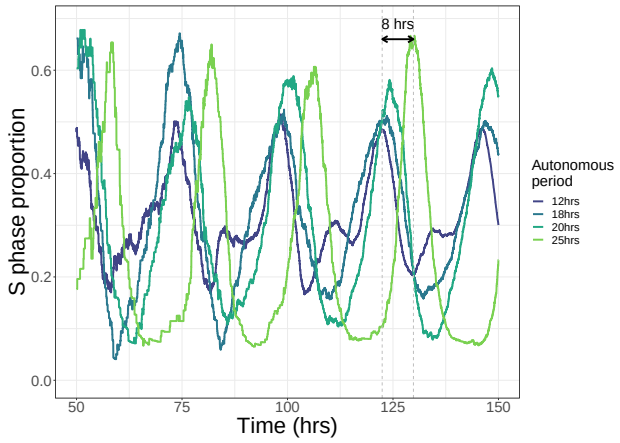

Figure 4.14: The variation of the proportion of cells in the S phase for cells cycling with autonomous periods of 12, 18, 20 and 25 hours. The S phase peak of cells with an autonomous period of 25 hours comes 8 hours after that of cells with an intrinsic cycling period of 12 hours.

4.3 G_1 proportion oscillations using DAPI imaging

The proportion of cells in each cell cycle phase can be obtained from the DAPI intensity profiles of a mixed population of cells, which typically shows a bimodal distribution. Cells in the G_1 phase (having lower nucleic acid content) contribute to the lower intensity mode while the S, G_2 and M cells (having double the nucleic acid content) contribute to the higher intensity mode. Fitting this DAPI intensity profile to a univariate normal mixture model allows us to find the proportion of cells in each phase of the cell cycle (Ferro *et al.* (2017), Dhuppar and Mazumder (2018)).

Since the lower intensity mode directly gives the G_1 phase proportion, it is the most convenient to study. To look at the variation of G_1 phase proportion over time, I seeded HCT116 cells in 34 35mm punched dishes with 1.5mm coverslip ($\sim$ 70,000 cells/dish) and synchronized 17 plates using 100nM Dexamethasone at the start of the experiment, leaving the rest unsynchronized. Post synchronization, I allowed all cultures to grow normally and fixed a synchronized and an unsynchronized culture every 3 hours using 4% PFA, obtaining a sequence of cultures fixed at different time points varying from 0 to 48 hours with a step size of 3 hours. I DAPI stained and imaged them to obtain DAPI intensity profiles for each time point. I fit the DAPI intensity profile for each field of view to a univariate normal mixture model to obtain its G_1 phase proportion.

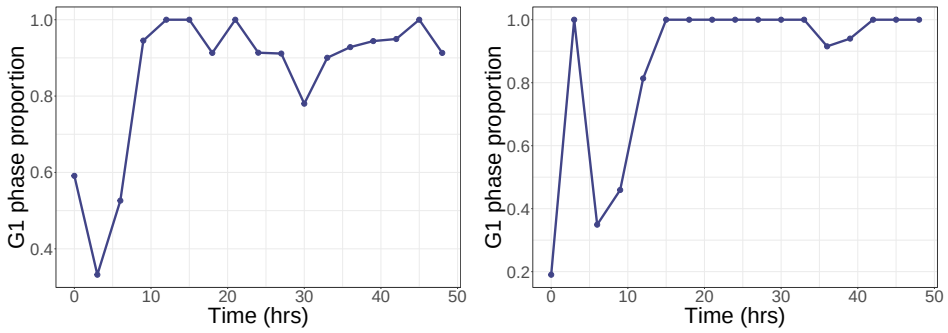

Figure 4.15: Variation in G_1 phase proportion with time (top: unsynchronized, left: synchronized). The phase proportion shows small variations in the asynchronous population and no variation in the synchronous population.

The proportion of cells in the G_1 phase shows a small amplitude oscillation that is not circadian in nature in the asynchronous cultures (Fig 4.15). In

both cultures, we see an initial short-period oscillation in the proportion of cells in the G_1 phase, which dies after one oscillation. Neither of the cultures shows a sustained oscillatory pattern in the G_1 proportion. One also notices that in the synchronous population, almost all time points starting from 18 hrs show a G_1 proportion of 1. This likely results from the nature of the total DAPI intensity profile from each time point (Fig 4.16), which is fit by a single normal distribution. In the mixture model, if the mean of the single normal distribution that fits the entire data falls below 1.7, then the G_1 proportion is set to 1 and is set to 0 otherwise.

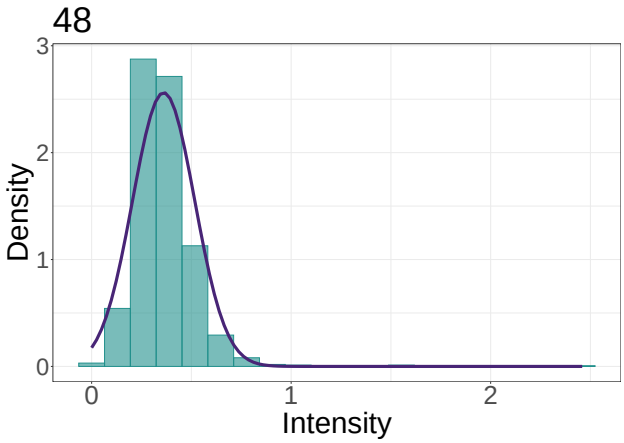

Figure 4.16: Total DAPI intensity profile for the last timepoint in the synchronized culture. The purple line is the fit given by the mixture model.

On carefully analyzing the mean intensity of the nuclei, I noticed that a large number of cells had a bright fluorescence. Fig 4.17 shows the average intensity of the pooled data from all time points for the synchronous and asynchronous population. The last bin has many cells, suggesting that the dynamic range of the microscope is smaller than the output fluorescence. To test this hypothesis, I reimaged the unsynchronized dishes for time points between 24hrs to 48hrs with a lower input LED light intensity, ensuring that the output fluorescence falls within the dynamic range of the microscope.

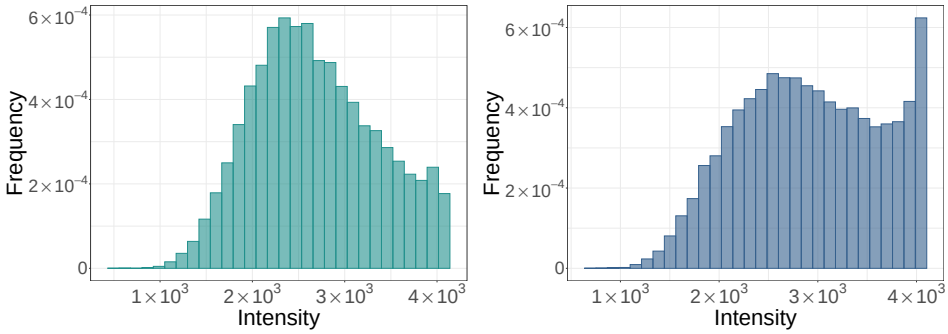

Figure 4.17: Mean DAPI intensity profile for all time points combined (left: unsynchronized, right: synchronized). The lack of a right tail suggests that the output fluorescence is brighter than the dynamic range of the microscope.

As shown in Fig 4.18, the mean DAPI intensity profile has a tapering right tail. Thus, the output fluorescence is within the dynamic range of the microscope.

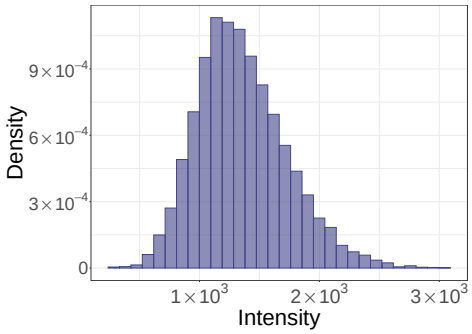

Figure 4.18: Variation of the G_1 proportion of asynchronous cells that were reimaged with a lower DAPI intensity profile.

The G_1 proportions obtained from the reimaged data (Fig 4.21) for the asynchronous population shows a very short period variation ($\sim$ 8.5 hrs detected by `ODeGP`) and do not show oscillatory behavior.

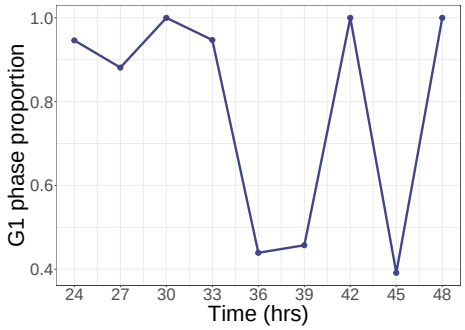

Figure 4.19: Variation of the G_1 proportion of asynchronous cells that were reimaged with a lower DAPI intensity profile.

An issue that still persisted, however, is that the total DAPI intensity does not always follow a bimodal distribution, where the second peak has a mean that is twice the first one. We found that this was particularly true for the early time points. For example, the histograms of the total DAPI intensity for the 24^{th} hour and 45^{th} hour time points are shown in Fig 4.20. The 24 hr timepoint data does not show bimodality, while the 45 hr one does. Most of the time points show a DAPI profile with an intermediate distribution wherein the bimodality is unclear because of noise (4.21). While such data can be fit by a mixture mode, it often leads to poor fits, as discussed later.

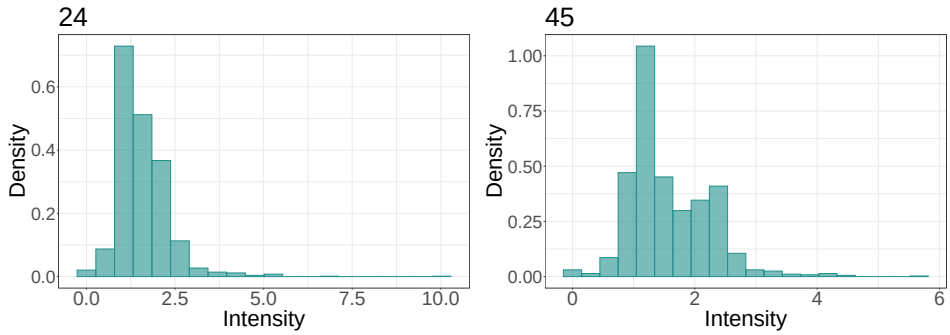

Figure 4.20: Total DAPI intensity profile for the 24^{th} hr (left) and the 45^{th} hr (right) time points obtained after re-imaging the dishes from the previous experiment with lower input LED intensity. The 24^{th} hr time point shows a single peak, while the 45^{th} hr time point shows two peaks.

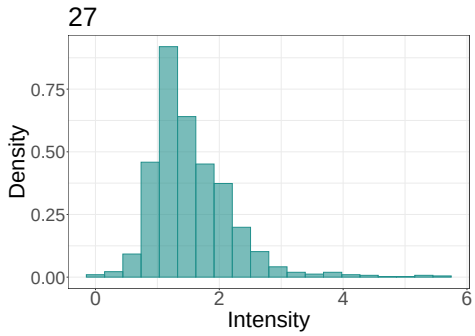

Figure 4.21: Total DAPI profile of the 27^{th} hr time point obtained after re-imaging. We see a right tail in the histogram, but we do not see two peaks.

The lack of a clear bimodal distribution has not been reported in the literature. Lack of bimodality can lead to the `flexmix` package fitting the data with a single normal distribution. Since we observed better bimodality at later time points compared to earlier ones, I re-ran my experiment with a slight modification. After seeding my cells in the 35mm punched plates, I let them grow for 48 hrs before beginning the experiment. This was done to allow the transients in phase proportion oscillations to die out. After 48 hrs, I synchronized half of the plates with 100nM Dexamethasone and repeated the experiment as before, with a time interval of 4 hours. While imaging the cells, care was taken that the input LED intensity was set appropriately and that the images were taken from different parts of each plate.

Contrary to what we expected, the DAPI profiles from this experiment were similar to those obtained in the re-imaged data as before (Fig4.22). Most of the time points did not show clear two peaks in the total DAPI intensity profile. The only timepoint that showed two peaks clearly is the last timepoint in the unsynchronized culture (Fig4.22).

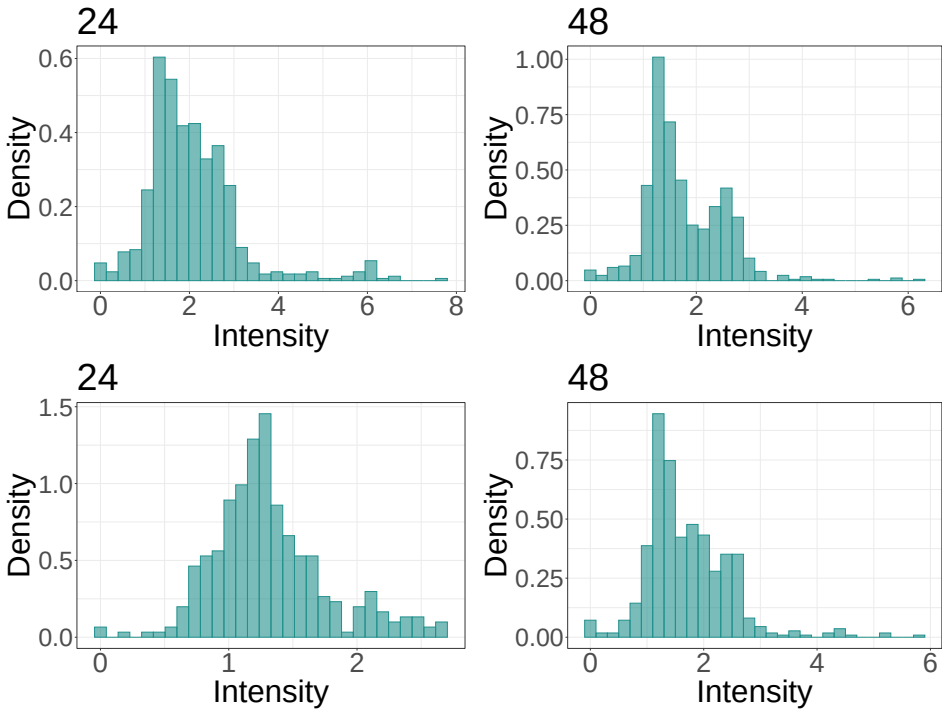

Figure 4.22: Total DAPI intensity profile for the unsynchronized culture (top) and the synchronized culture (bottom). The time point is indicated at the top left of each plot.

The resultant G_1 proportions obtained by fitting the data with the mixture model did not show any oscillatory pattern (Bayes factor of 0.57 for the asynchronous population and 0.94 for the synchronous one)(Fig 4.23). We see a random variation in the G_1 proportion in both cultures.

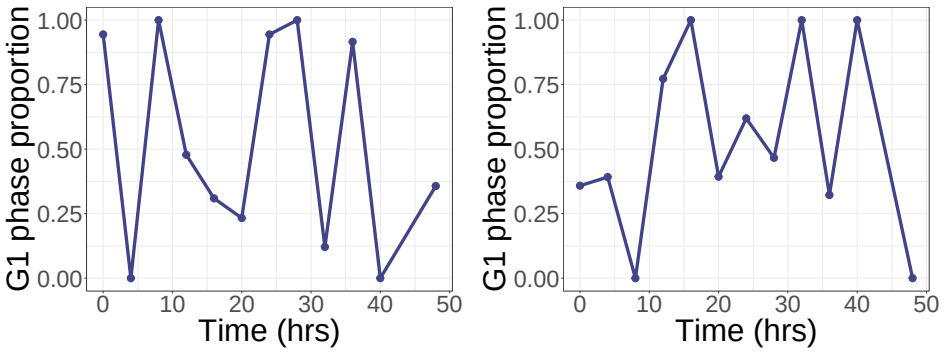

Figure 4.23: Variation in the proportion of cells in the G_1 phase with time for the unsynchronized (left) and synchronized (right) cultures.

To check if what we were observing was not a chance event, I repeated my experiment with a new set of cultures, keeping the experimental setup the same. The DAPI intensity profile for these cultures did not show a clear bimodality for any time point in either culture. For example, the 24 and 48 hr time points are shown in Fig 4.24. There is a single mode with a right tail in each case.

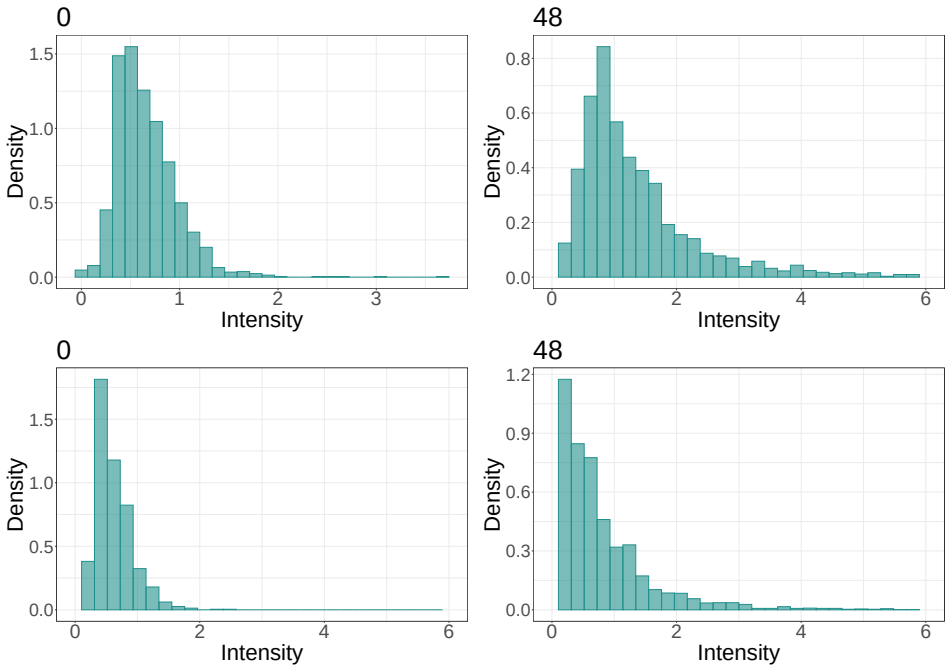

Figure 4.24: Total DAPI intensity profile for the unsynchronized culture (top) and the synchronized culture (bottom) in the repeat experiment. The time points are indicated in the top-left of each plot.

The total DAPI intensity profile for each time point was fit to a mixture model to get its G_1 proportion. Neither cultures show a periodic variation in the G_1 proportion (Fig 4.25). The rhythmicity of the G_1 proportion variation for each culture was checked using `ODeGP`. Neither culture returned an oscillatory pattern in the G_1 proportion (Bayes factor 0.76 for the unsynchronized population and 6.19 for the synchronized one). However, we notice that the fraction of cells in the G_1 phase shows a single oscillation in the synchronized culture having a period of at least 20 hours. Following that, the G_1 proportion begins to vary randomly. The lack of periodicity detection by `ODeGP` could be due to the second half of the data, which shows random variations. To test this, I subset the G_1 proportion data for both cultures to include data until the 28^{th} hr time point. I analyzed its rhythmicity using `ODeGP`. The algorithm predicts that the proportion of cells in the G_1 phase oscillates in the synchronized culture with a period of 25.8 hours (Bayes factor 40), while it shows no oscillation in the unsynchronized population (Bayes factor 0.97) (Fig 4.26).

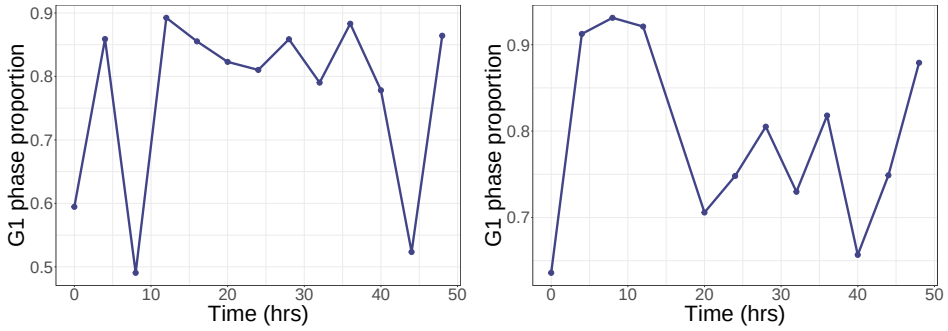

Figure 4.25: Variation in the proportion of cells in the G_1 phase with time for the unsynchronized (left) and synchronized (right) cultures in the repeat experiment.

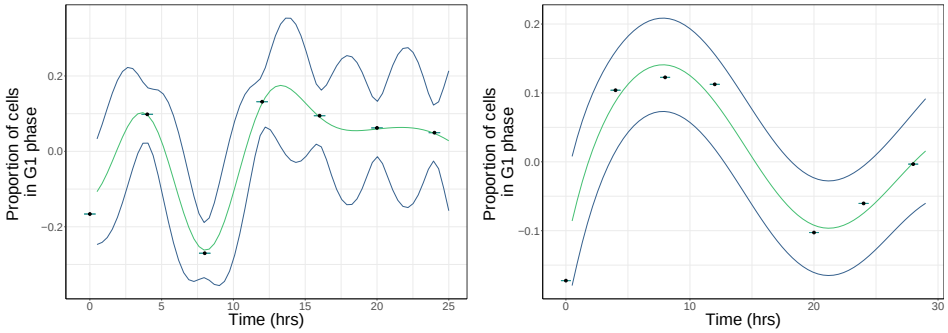

Figure 4.26: Rhythmicity analysis for the variation of G_1 proportion up till the 28 hr time point. The unsynchronized culture (left) shows no oscillations (Bayes factor 0.97), while the synchronized population shows an oscillation with a period of 25.8 hours (Bayes factor 40.07). The green line is the posterior mean of the fit, and the blue line is the standard deviation. The data is centered around zero by subtracting its mean.

The period of oscillation in the G_1 proportion in the synchronized culture during the initial half of the experiment is longer than 24 hours. This could likely be due to Dexamethasone treatment, which is known to slow down cell growth by increasing G_1 arrest. In fact, the initial increase in G_1 proportion is consistent with what we expect the cell cycle phase to be post-Dexamethasone treatment.

A question that still was not answered was the lack of two peaks in the histograms of the DAPI intensities for each time point. A single peak with a tail could result from a very short G_2/M phase. In order to validate this, we used Flow cytometry to check the fraction of cells in each cell cycle phase.

4.3.1 Flow cytometry

We first ran a control experiment where we cultured HCT116 and NIH3T3 cells in a T25 flask and harvested them using 0.05% and 0.25% Trypsin, respectively. A million cells (10^6 cells) from each culture were DAPI stained and loaded in a cytometer. The fluorescence data is shown in Fig 4.27, and the fraction of cells in each cell cycle phase is given in Table 4.1.

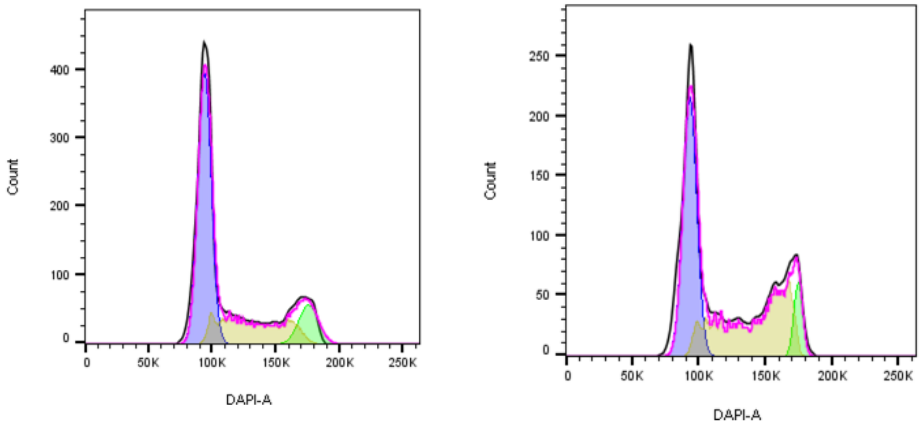

Figure 4.27: DAPI fluorescence observed in the flow cytometry test experiment. The figure on the left is for NIH3T3 cells, and the figure on the right is for HCT116 cells.

Phase	NIH3T3	HCT116
G_1	59.6%	45.0%
S	29.2%	45.1%
G_2	12.6%	8.15%

Table 4.1: Distribution of cells in each cell cycle phase in NIH3T3 and HCT116 cells obtained from flow cytometry of DAPI stained cells.

The DAPI intensity profile does show two peaks in both cultures. Interestingly, the fraction of cells in the G_1 and S phase is similar in HCT116 cells, whereas this is not the case in NIH3T3 cells. This might be due to a higher proliferating population in HCT116 cells,

To validate our imaging-based G_1 proportion data, we ran a timepoint-based experiment for HCT116 cells for flow cytometry. Cells were grown in 35mm cell culture-treated dishes for 48 hours. Half of the plates were

synchronized with 100nM Dexamethasone, and the remaining were left untreated. Two plates, one from each culture, were fixed every four hours for flow cytometry using ethanol and an RNase buffer. These were then stained with PI and loaded onto a cytometer. The output fluorescence profiles are shown in Fig 4.28.

The fraction of cells in the G_1 phase is lower than that in the S phase across all time points and cultures. Furthermore, there is no oscillation in the fraction of cells in each cell cycle phase (4.28). We notice that the average fraction of cells in the G_1 phase rises over the 48 hours for both the culture types. Similarly, the fraction of cells in the S phase decreases with time. This might be due to the loss of synchrony in cells over time, leading to the phase proportions settling to a steady state value. It could also likely result from an increase in the G_1 duration that occurs with increased cell density.

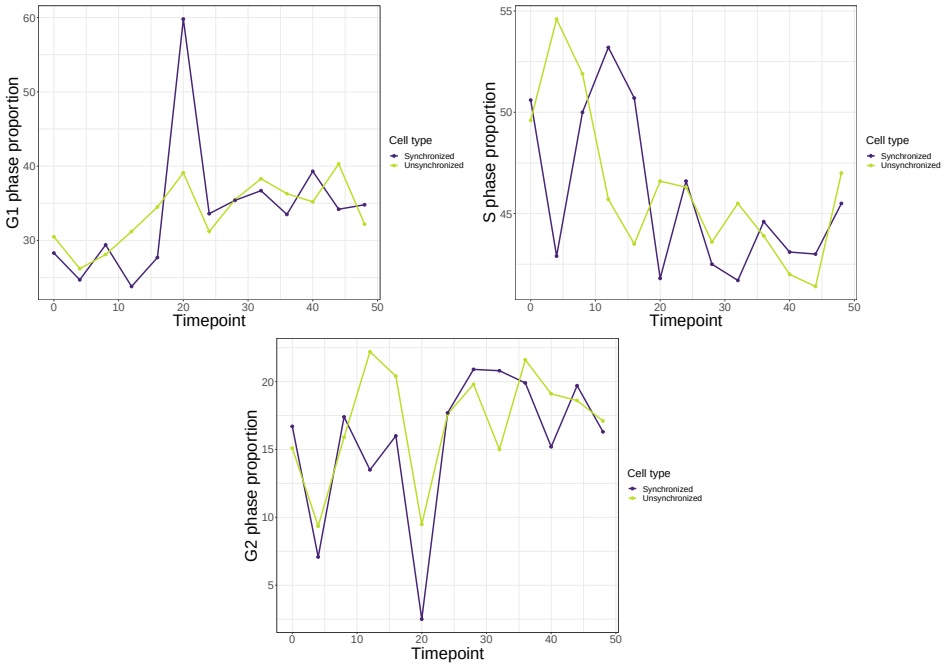

Figure 4.28: Fraction of cells in each cell cycle phase obtained from the flow cytometry data.

While the dip in proportion of all cell cycle phases at the 20^{th} hour in the synchronized population might make it look like there is an oscillatory pattern in the S phase proportion, there is a large apoptotic population (28.37%) in that sample.

The flow cytometry experiment needs more standardization regarding the seeding of cells, the incubation period before beginning the experiment,

and the DAPI and PI staining protocol. However, for our imaging-based DAPI experiment, it is noteworthy to note that we see two peaks in the fluorescence data of DAPI and PI. Thus, in our imaging-based cell cycle staging technique, we must ensure that our image acquisition and analysis give us DAPI intensities comparable to flow cytometry data to assign the cell cycle stages properly. Furthermore, a large S phase population likely makes the gap between the two peaks in imaging-based DAPI profiles difficult to identify, as the S phase cells would have DAPI intensities in that region.

4.4 Reconstructing the PRC of the cell cycle oscillator

The phase difference between the cell cycle phase proportions of cells with different intrinsic periods can be theoretically predicted using the Kuramto model (Eqn 2.21). However, to apply the Kuramoto model to the clock-cell cycle system, we need to know the nature of coupling (i.e., the PRC) between the two oscillators. To do this, I aimed to use the algorithm given by Cestnik and Rosenblum (2018) to infer the PRC of a continuously perturbed oscillator.

I began by developing a code in R that implemented the algorithm given by Cestnik and Rosenblum (2018). To test my code, I ran a simulation using a known PRC function (Eqn 2.29) and spike data, similar to Fig 1(b) in Cestnik and Rosenblum (2018). The perturbation amplitude (ϵ) was set to 7.6, and the correlation time was set to 0.1. However, the PRC reconstruction algorithm that I wrote did not return a good estimate for the true PRC after 10 iterations (4.29), having a Δ_Z value of 0.37. In fact, the PRC was not reconstructed well even by the code available online from the publication (Fig 4.29).

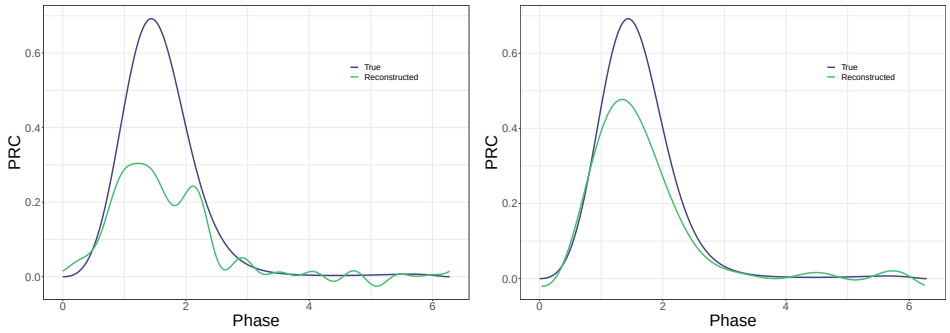

Figure 4.29: Reconstructed PRC using the algorithm given by Cestnik and Rosenblum (2018). The perturbation amplitude (ϵ) and correlation time (τ) are 7.6 and 0.1. On the left is the reconstruction using the R code I have written, and on the right is the reconstruction using the code available online. The reconstruction error (Δ_Z) for the R code is 0.37, and that for the code available online is 0.20.

I also ran the algorithm I wrote for a less perturbed oscillator with a perturbation strength (ϵ) of 6 and a correlation time (τ) of 0.01. The code I wrote could reconstruct the PRC accurately ($\Delta_Z = 0.01$).

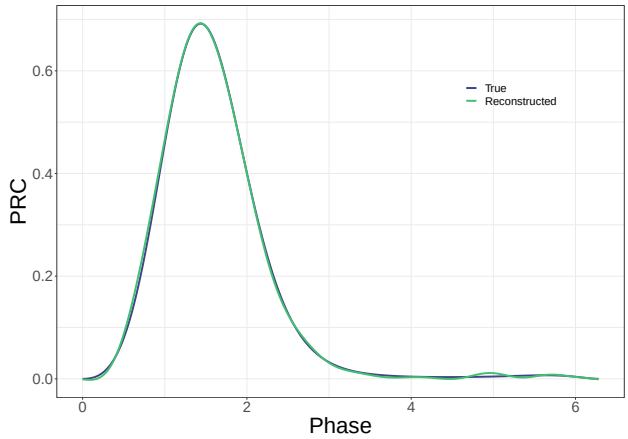

Figure 4.30: Reconstructed PRC for a perturbation amplitude (ϵ) 6 and correlation time (τ) 0.1. The error in reconstruction (Δ_Z) is 0.01.

4.5 Radiation model

The four-compartment model suggests that cells that cycle with different autonomous periods show a phase shift in their cell cycle oscillations (Fig

4.14). Thus, it is imperative that we extend this model to incorporate the effect of radiation on the cells and understand the effects of different radiation schemes. I developed a radiation simulation using the model described by Powathil *et al.* (2013). Using this simulation, I looked at the effect of radiation on the cell cycle oscillations for different doses and cell types.

4.5.1 The fraction of cells killed is cell cycle phase dependent

An important aspect of the radiation model is phase-specific radiosensitivity. In the modified LQ model (Eqn 2.13), the phase-specific sensitivity is given the the constant γ. The expected trend of cell death should be M $>$ G_2 $>$ G_1 $>$ S. In order to verify if the expected trend of cell death is seen, I ran a simulation with cells having an autonomous period of 18 hours and irradiated them with 2 Gy at time 80. I did this for cells that were not clock coupled and cells that had a clock coupling of 0.5. Firstly, we note that the cell cycle components cycle normally until the cell is irradiated, after which the MPF concentration is held fixed for a randomly sampled duration with a mean of 18 hours and a standard deviation of 4 hours (Fig 4.31). The clock continues to oscillate normally even post-radiation.

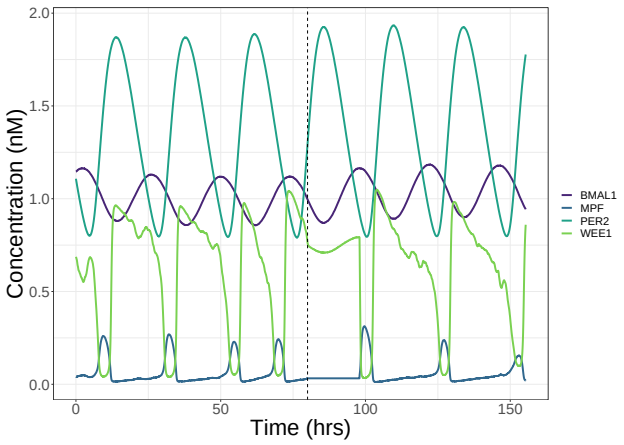

Figure 4.31: Clock and cell cycle gene expression oscillations obtained from the radiation simulation. The autonomous period of the cell is 18 hours and we apply a dosage of 2 Gy at time 80 (indicated by the dotted line).

Furthermore, the number of cells that die post-radiation follows the expected trends for the clock coupled as well as the clock uncoupled case (Fig 4.32).

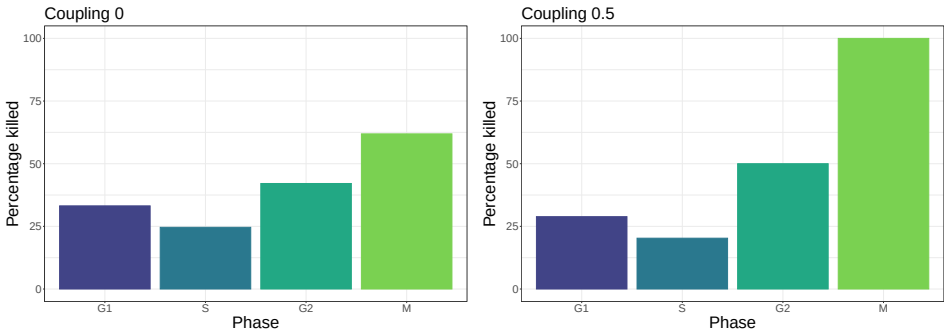

Figure 4.32: Percentage of cell death post radiation in the clock-uncoupled (left) and the clock-coupled (right) cases.

4.5.2 Higher dosage leads to higher cell kill

I checked the effect of increasing the radiation dosage on cells that cycle with an autonomous period of 18 hours with a clock coupling of 0.5. I irradiated these cells with doses of 2 Gy, 4 Gy, 6 Gy, and 10 Gy at time 80 and looked at their total population reduction. As shown in Fig 4.36, the number of cells drops as the dose increases. Post-radiation, we see an increase in the population. This happens because the cell cycle returns back to normal after the G_1 arrest in the simulation.

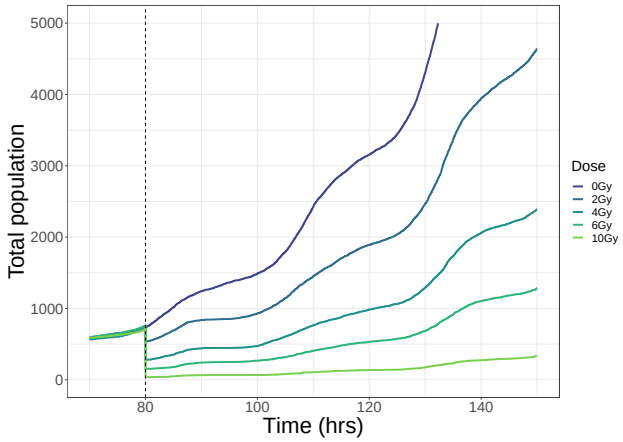

Figure 4.33: Increase in radiation dosage leads to higher cell killing. The autonomous period of the cell is 18 hours, and we apply a radiation dose of 2 Gy at time 80 (indicated by the dotted line).

4.5.3 The G_1 proportion rises post radiation

In my simulation, cells show G_1 arrest post-radiation. Thus, we expect the cells in the S/G_2 phase to divide and get arrested in the G_1 phase, leading to an accumulation of cells in this phase. Indeed, we see a peak in the fraction of cells in the G_1 phase post tradition (Fig 4.34). Interestingly, there are two G_1 peaks. The earlier peak arises from the cells irradiated in the $S/G_2/M$ phase, which get arrested in the G_1 phase after division. We see a drop in the G_1 proportion around time 100, which results from the cell cycle release of those cells that were irradiated in the G_1 phase. These cells divide and contribute to the second G_1 peak. Finally, the cells irradiated in the $S/G_2/M$ phase are released from cell cycle arrest, and the cell phase proportions oscillate normally.

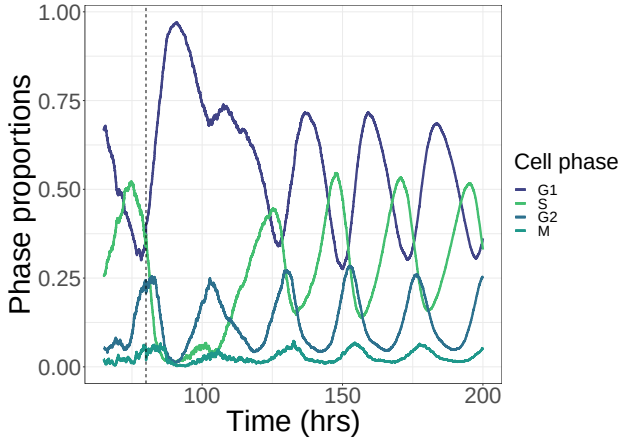

Figure 4.34: Variation of cell phase proportions post-radiation. The autonomous period of the cell is 18 hours, and we apply a dosage of 2 Gy at time 80 (indicated by the dotted line). After irradiating the cells, we observe two peaks in the G_1 phase proportion.

I compared the G_1 proportion oscillation for irradiated cells with the unirradiated cells and observed that irradiation leads to a temporary phase shift in the G_1 peak. The irradiated cells skip one oscillatory division cycle and start oscillating normally afterward (Fig 4.35).

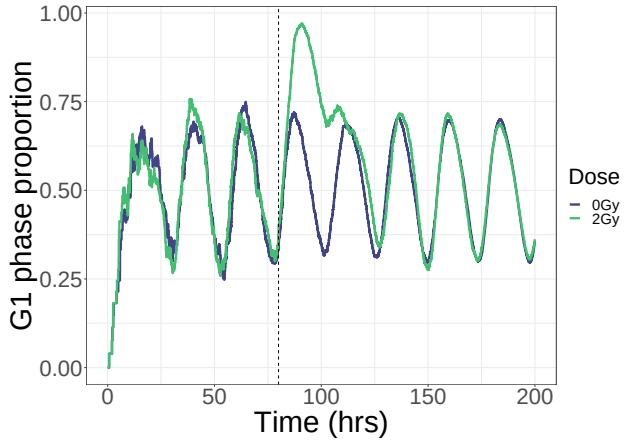

Figure 4.35: Comparison of the G_1 proportion oscillations shown in Fig 4.34 with unirradiated cells. The radiated cells accumulate in the G_1 phase and skip one division cycle. The dotted line indicates the time of irradiation.

4.5.4 Radiation synchronizes the cell cycle

The rise in the fraction of cells in the G_1 proportion could possibly serve as a synchronization of cancer cells. To test this, I started with an asynchronous cell population that is not coupled to the clock. Thus, these cells would not show any cell phase proportion oscillations independently. I irradiated these cells at time 80 with a dose of 2 Gy and observed the cell phase dynamics post-radiation.

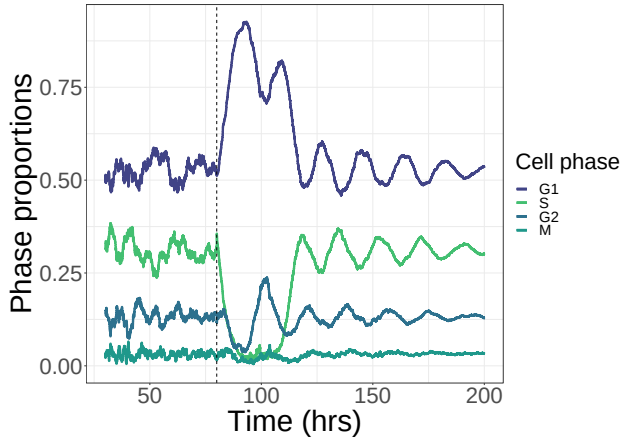

Figure 4.36: The cell proportions show oscillation post-radiation even in cells not coupled to the clock. The autonomous period of the cell is 18 hours, and we apply a dosage of 2 Gy at time 80 (indicated by the dotted line).

The cell phase proportions show damped oscillations post-radiation. In fact, these oscillations persist even 120 hours or 5 days after radiation. This suggests that the radiation synchronizes the cell cycle phases, which eventually get unsynchronized due to the variance in cell cycle durations. The duration for which the synchrony is maintained would depend on the cell cycle arrest duration post-radiation.

4.5.5 Time to first division post radiation shows a bimodal distribution

The fraction of cells in the G_1 phase shows two peaks post-radiation, with the first peak resulting from cells in the $S/G_2/M$ phase and the second peak resulting from cells in the G_1 phase. In fact, if we check the time to division post-radiation, we see that it follows a bimodal distribution (Fig 4.37). This result agrees with experimental data obtained by Reyes *et al.* (2018), who studied G_1 phase arrest post-radiation in RPE-hTERT cells.

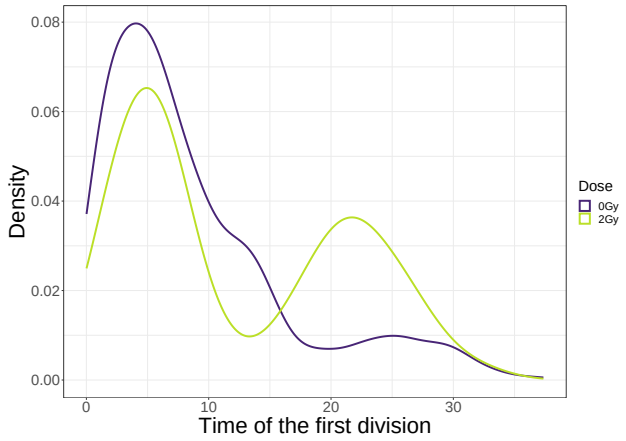

Figure 4.37: The time to the first division of irradiated cells follows a bimodal distribution.

The first peak in the above figure results from the early dividing cells, which were irradiated in the $S/G_2/M$ phase, while the second peak arises from the late dividers, which were irradiated in the G_1 phase.

4.5.6 Time of irradiation affects total population

The central question in chronotherapy is to understand the effect of irradiating cells at different times of the day. We expect that irradiating cells when most of them are in the M phase should cause maximal damage. To test this,

I ran a set of simulations where I irradiated cells at different times, corresponding to their S peak, G_2 peak, G_2/M peak, and M peak. I looked at the relative decrease in the total population post-radiation. We see that when cells were irradiated at the G_2/M peak, they showed the greatest population drop, followed by cells irradiated at the M peak, G_2 peak, and then the S peak (Fig 4.38). The higher drop in total population of cells irradiated when most cells are in the G_2/M phase is likely because a higher fraction of cells are in the G_2 phase, even if it is slightly less sensitive than the M phase. This suggests that timing radiotherapy should consider not only the differential radiosensitivities of the cell cycle stages but also the number of cells in each stage.

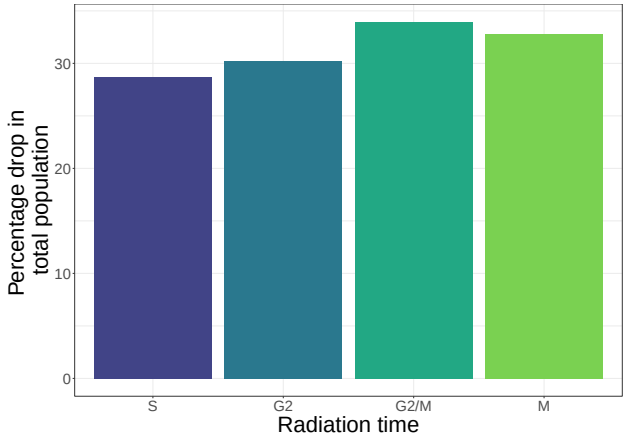

Figure 4.38: Percentage drop in the total populations of cells that were irradiated at different times corresponding to their S peak, G_2 peak, G_2/M peak, and M peak. In all cases, the cells were dosed with 2Gy of radiation.

Chapter 5

Discussion

The coupling between the circadian clock and the cell cycle is known to give rise to cell cycle entrainment. Furthermore, chronotherapy aims to exploit this coupling to cause maximal damage to cancer cells while minimizing the toxicity to normal cells. In this study, I used an interdisciplinary approach to understand how the clock coupling to the cell cycle at a molecular level can give rise to population dynamics. I further looked into how the population dynamics change on irradiating the cells. The central theme of these studies is to understand a way to develop an optimal radiation chronotherapy scheme for cancer.

5.1 Molecular clock coupling leads to oscillation in cell phase proportions

In the absence of external perturbation, the fraction of cells in each cell cycle phase should settle to a constant value predicted by Eqn 4.1. However, multiple studies have reported circadian oscillation in cellular proliferation (Kiessling *et al.*, 2017). The circadian clock entrains the cell cycle via the regulatory influence of WEE1 on MPF (Matsuo *et al.*, 2003). In my study, I looked at a computational way to combine molecule dynamics of the clock TTFL and the cell cycle genes with population-level dynamics to look at emergent phenomena. I developed a three-compartment lineage-generating simulation using the mathematical framework proposed by El Cheikh *et al.* (2014). The compartments in this simulation represent the G_1, S/G_2 and M phases. Transition through the cell cycle phases is governed by the MPF concentration in each cell. Thus, this model can replicate the molecular oscillations of the clock and cell cycle genes and simulate cell division and population growth (Fig 4.1).

Our model shows that the fraction of cells in each cell cycle phase shows sustained oscillations only when the clock is coupled to the cell cycle (Fig 4.4). Furthermore, the period of these oscillations is $\sim$ 24 hours (Fig 4.5), suggesting an entertainment of global cell cycle behavior by cellular clocks. An interesting observation from the simulation is that the period of the phase proportion oscillations remains the same regardless of the coupling strength (Fig 4.9). Similar observations were made by El Cheikh *et al.* (2014) when they compared their model with models given by Mirsky *et al.* (2009) and Leloup and Goldbeter (2004). They noted that the cell cycle need not be phase-locked with the clock in a 1:1 ratio across different autonomous cell cycle durations. The entrainment of the cell cycle to the clock can follow a rational ratio $n : m$, such that n divisions occur at the end of m cycles of the clock. The entrained cell cycle period is the same for certain autonomous cell cycle periods, regardless of coupling. Since our simulations have been run with autonomous periods of 20 hrs, the 24-hour entrainment of the cell phase proportions is because of this phase-locking phenomenon. However, one must note that the amplitude of these oscillations increases with coupling, indicating higher synchronicity between cells at higher coupling values. Thus, while the dominant oscillatory frequency is 24 hours in oscillation of the phase proportions, it is the strongest period of oscillation only in highly coupled cases.

Modeling the effect of radiation on the cell population in a cell phase-dependent manner requires better cell phase resolution. The sensitivity of the S phase cells is lower than that of the G_2 phase. Thus, I developed a four-compartment model that uses the same clock dynamics of the three-compartment model but has re-parametrized cell cycle oscillations that agree with experimental observations. The resultant simulation can recapitulate the cell cycle phase durations typically observed for a proliferative human cell (Fig 4.11).

The four-compartment model also suggests that the fraction of cells in each cell cycle phase shows an oscillatory pattern on clock coupling, with an oscillation period of 24 hours (Figs 4.12 and 4.13). The variation of the proportion of cells in each cell cycle phase has not been studied much in HCT116 cells. Thus, we turned to imaging-based cell cycle staging using DAPI stains. DAPI fluorescence can be used to quantify the DNA content of a cell. Thus, DAPI data can be fit to a univariate normal mixture model to get the fraction of cells in the G_1 and $S/G_2/M$ phase.

We studied the variation of G_1 proportion in HCT116 over time by seeding multiple 35mm dishes and fixing and DAPI staining them at different time points. Every experiment had two types of cultures - one set of dishes was treated with 100 nM Dexamethasone for 1 hour, while the other set was left

untreated. Dexamethasone promoted *Per2* transcription and leads to cell cycle synchronization in the G_1 phase (Kiessling *et al.*, 2017).

Our experiments using fluorescence imaging for cell cycle staging highlighted some important points that should be taken care of while performing this experiment. Firstly, we need to ensure that the cells are seeded at a density that does not lead to over-confluence of cells over the course of the experiment, as this can lead to longer G_1 phase durations. Secondly, it is important to choose a DAPI concentration that does not lead to the output DAPI fluorescence exceeding the dynamic range of the microscope. We used 1 μg/mL of DAPI in all our experiments. Thirdly, the input LED intensity of the microscope should be set according to its dynamics range. It is also important to set the Z-stacks according to the size of the nucleus of the cells. The Z-stacks are acquired such that the nuclei are not entirely out of focus in any stack, as this will contribute to noise during image analysis. Lastly, it is important to image cells from all parts of the plate to prevent biases in sampling that might occur while imaging only in a certain region.

The total DAPI intensity profiles that we have obtained across different experiments suggest that we rarely observe two peaks in the profiles. While this is expected in synchronized cultures, it is initially strange to observe single peaks in unsynchronized cultures. This could arise from possible synchronicity that persists in our population, regardless of Dexamethasone treatment. However, the synchronicity is observed in the asynchronous population as well. This seems unlikely since we grow both cultures for 48 hours to offset any cell cycle synchronicity that arises due to trypsinization and cell seeding. The other hypothesis is that a significant population of cells are in the G_1/S phase compared to the G_2/M phase, leading to a very prominent first peak and lack of a clear second peak. This hypothesis can be tested by using a G_2 arrest drug like Ginkgetin (Lee *et al.*, 2017) and observing the cell cycle dynamics post-drug release. A prominently G_1/S population is likely to result from a longer G_1 and S phase duration in the cell cycle. Literature on the exact cell cycle phase durations for HCT116 cells shows slight variability depending on the technique used. G_1 phase durations are typically in the range of 4.1-5.4 hours (Pereira *et al.* (2017), Bernard *et al.* (2019)). The literature on S phase duration has a lot of variability. Measurements made from EdU or flow cytometry revealed that the duration of the S phase is 5-7.1 hours (Pereira *et al.*, 2017), while a dual EdU-BrdU pulse-chase method reports an S phase duration of 11.7 hours (Bialic *et al.*, 2022). Nevertheless, we expect a higher proportion of cells to be in these phases, implying that the DAPI peaks we see at each time point would mostly be unimodal. Furthermore, our flow cytometry data agrees with the trend of the S phase being longer than the G_1 phase in HCT116 cells in the unsynchronized cultures.

Synchronizing the cultures using Dexamethasone would lead to a spike in the fraction of cells in the G_1 phase, at least during the initial time points. We only see this in the last experiment. Furthermore, we observe that the G_1 phase proportion shows an oscillation of a period of 25.8 hours during the first 28 hours (Fig 4.26). This circadian oscillatory pattern dies out after 28 hours. Loss of synchrony due to noise could contribute to a dying oscillatory pattern over time, suggesting that an extrinsic synchronizer is needed to maintain sustained oscillations in the phase proportions. This suggests that the fraction of cells in each cell cycle phase does show circadian rhythmicity. However, multiple biological replicates will be required to test this rigorously.

The flow cytometry data shows no oscillatory pattern in any phase proportion variation in either cell type (Fig 4.26). Furthermore, we do not see a spike in the G_1 proportion after Dexamethasone treatment. This is quite surprising and is likely due to a high fraction of apoptotic cells, especially in the 4^{th} hour. Furthermore, we see a gradual increase in the G_1 proportion and a drop in the S proportion with time. This could result from increased cell confluence with time, leading to G_1 phase duration lengthening (Bernard *et al.*, 2019). To offset the effect of cell density with time, we can seed cells at different starting densities to ensure that the cell densities at the time of fixing are constant.

5.2 Phase-shifted cell cycle oscillations in cells with varying intrinsic periods

To test how cancer and normal cell cycle dynamics vary in a clock-coupled system, we used the three-compartment model to simulate cell cycle dynamics of clock-coupled cells having autonomous cell cycle periods 18, 20, 25, and 26. While the fraction of cells in the M phase oscillates with a circadian period, we see peaks in the oscillation patterns at different times for the different cell types (Fig 4.10). The cells with an autonomous period of 26 hours show a phase delay of 5.6 hrs in the M phase proportion oscillations compared to the cells that cycle at 18 hrs. As the autonomous cell cycle period rises, the M phase proportion oscillations show a phase delay in their oscillation pattern. We also notice an increase in the amplitude of the M phase proportion oscillation with the autonomous period. This is due to an increase in synchronicity in cells that intrinsically cycle with a period close to the period of the circadian clock. Similar patterns are seen in the four-compartment model (Fig 4.14). The phase shift in cell cycle phase proportion dynamics between different cell types is of major interest. It

holds the potential to be exploited by chronotherapy, wherein we radiate cancer cells based on the time of day when a majority of them are in the M phase. Since this M phase peak would appear at a time different from that of normal cells, the chronomodulated radiotherapy would cause greater damage to cancer cells than normal cells. Theoretical predictions of the phase difference between the M phase peak of cancer cells and normal cells would help us set a bound on the therapeutic window available during a day during which radiotherapy would be most impactful.

I turned to the Kuramoto model for couple oscillators to understand the phase difference in phase proportion variation between different cell types. While this model has been extensively studied and applied in the context of the circadian clock (Granada *et al.*, 2013), its application in the circadian clock-cell cycle coupled oscillator system is limited due to a poor understanding of the coupling between the two. Kuramoto's analysis was mainly done for a sinusoidal coupling between the oscillators (Kuramoto, 1984). However, no data suggests that the cell cycle responds to perturbations by the clock in a sinusoidal manner. Thus, obtaining a Phase Response Curve (PRC) for this coupled oscillator system is important. This study proves to be challenging since the clock cannot discretely and infinitesimally perturb the cell cycle. I turned towards the algorithm given by Cestnik and Rosenblum (2018) to infer the PRC of this coupled oscillator system from time series data. While the algorithm itself has its issues in reconstructing the true PRC (Fig 4.29), there are further concerns about using this algorithm to infer the PRC of this system. Since the clock is coupled to the cell cycle quite strongly, the cell cycle reporter level(MPF in the simulation) is highly correlated to the clock level. This makes inferring the PRC an issue since there is not enough variability in the phase at which a particular clock perturbation arrives at the cell cycle reporter. I had an email discussion on this issue with Rok Cestnik, who suggested a simplification of a neural network approach where we train a neural network to predict the response of an oscillator to an input perturbation depending on the phase it arrives at. Thus, developing a new way to infer the PRC of the cell cycle oscillator is a challenge that needs more thought and work.

5.3 Dosage timing can be studied using the radiation model

The radiation model that I have developed can be used to study the dose (Fig 4.36) and cell cycle phase-dependent effects of radiotherapy on cells. The

model is able to replicate the experimentally obtained cell cycle death trends (Fig 4.32). Furthermore, we see an accumulation of cells in the G_1 phase post-radiation since we have only simulated a G_1 arrest in our model (Fig 4.35). While we can also simulate G_2 arrest as was done in Powathil *et al.* (2013), Reyes *et al.* (2018) only observed G_1 arrest in RPE-hTERT cells. Thus, we could validate our simulation by replicating the bimodal distribution of the time to the first division post-radiation that they experimentally studied (Fig 4.37).

The radiation simulation suggests that radiating cells when most of them are in the G_2/M phase can cause the most cell death (Fig 4.38). This agrees with experimental results (Sinclair and Morton (1965), Takane *et al.* (2000), Plikus *et al.* (2013)) and leads us to move on to develop a sequential dosage scheme that would allow us to reduce the tumor burden. Our simulation results suggest that the G_1 accumulation of cells post-radiation leads to the skipping of one normal cell division cycle (Fig 4.35). Furthermore, we observe that radiation can synchronize cells (Fig 4.36). From a therapy point of view, this means that the irradiated cells would not be very sensitive to a subsequent round of dosage for a period equal to the arrest duration. Current sequential radiotherapy schemes have looked at dosing consecutively for a certain number of days (Kapiteijn *et al.* (2001), Dean *et al.* (2022)). However, our model suggests that cell cycle arrest post-radiation would make cancer cells less sensitive to radiation-induced DNA damage, leading to higher toxicity effects compared to cancer cell death. Thus, it would be advisable to dose patients after the cancer cell's expected cell cycle arrest duration.

We can use the radiation simulation to understand how two different cell types co-evolve post-radiation. The LQ model parameters and cell cycle arrest durations would differ for the two cell types. We know that cells with different autonomous periods have an inherent phase difference in their cell cycles (Fig 4.14). Thus, it would be interesting to understand the change in the phase difference between the cell phase oscillations of these cell types before and after radiation.

References

Altinok A, Gonze D, Lévi F, Goldbeter A (2011), An automaton model for the cell cycle. *Interface Focus.* 36–47.

Balsalobre A, Damiola F, Schibler U (1998), A Serum Shock Induces Circadian Gene Expression in Mammalian Tissue Culture Cells. *Cell.* 929–937.

Becker-Weimann S, Wolf J, Herzel H, Kramer A (2004), Modeling Feedback Loops of the Mammalian Circadian Oscillator. *Biophysical Journal.* 3023–3034.

Bermúdez-Guzmán L, Blanco-Saborío A (2021), The Time for Chronotherapy in Radiation Oncology. *Frontiers in Oncology.*

Bernard D, Mondesert O, Gomes A, Duthen Y, Lobjois V, Cussat-Blanc S, Ducommun B (2019), A checkpoint-oriented cell cycle simulation model. *Cell Cycle.* 795–808.

Bialic M, Al Ahmad Nachar B, Koźlak M, Coulon V, Schwob E (2022), Measuring S-Phase Duration from Asynchronous Cells Using Dual EdU-BrdU Pulse-Chase Labeling Flow Cytometry.*Genes.* 408.

Bieler J, Cannavo R, Gustafson K, Gobet C, Gatfield D, Naef F (2014), Robust synchronization of coupled circadian and cell cycle oscillators in single mammalian cells. *Molecular Systems Biology.* 739.

Blake WJ, KAErn M, Cantor CR, Collins JJ (2003), Noise in eukaryotic gene expression. *Nature.* 633–637.

Breakspear M, Heitmann S, Daffertshofer A (2010), Generative Models of Cortical Oscillations: Neurobiological Implications of the Kuramoto Model. *Frontiers in Human Neuroscience.*

Buhr ED, Takahashi JS (2013), Molecular Components of the Mammalian Circadian Clock. Springer Berlin Heidelberg. 3–27.

Cestnik R, Rosenblum M (2018), Inferring the phase response curve from observation of a continuously perturbed oscillator. *Scientific Reports.* 13606.

Chakrabarti S, Michor F (2020), Circadian clock effects on cellular proliferation: Insights from theory and experiments. *Current Opinion in Cell Biology.* 17–26.

Chakrabarti S, Paek AL, Reyes J, Lasick KA, Lahav G, Michor F (2018), Hidden heterogeneity and circadian-controlled cell fate inferred from single cell lineages. *Nature Communications.* 5372.

Clairambault J, Gaubert S, Lepoutre T (2011), Circadian rhythm and cell population growth. *Mathematical and Computer Modelling.* 1558–1567.

Cooper GM (2000), The Eukaryotic Cell Cycle. Sinauer Associates.

Dean JA, Tanguturi SK, Cagney D, Shin KY, Youssef G, Aizer A, Rahman R, Hammoudeh L, Reardon D, Lee E, Dietrich J, Tamura K, Aoyagi M, Wickersham L, Wen PY, Catalano P, Haas-Kogan D, Alexander BM, Michor F (2022), Phase I study of a novel glioblastoma radiation therapy schedule exploiting cell-state plasticity. *Neuro-Oncology.* 1100–1112.

Dhuppar S, Mazumder A (2018), Measuring cell cycle-dependent DNA damage responses and p53 regulation on a cell-by-cell basis from image analysis. *Cell Cycle.* 1358–1371.

Diamantopoulou Z, Castro-Giner F, Schwab FD, Foerster C, Saini M, Budinjas S, Strittmatter K, Krol I, Seifert B, Heinzelmann-Schwarz V, Kurzeder C, Rochlitz C, Vetter M, Weber WP, Aceto N (2022), The metastatic spread of breast cancer accelerates during sleep. *Nature.* 156–162.

Droin C, Paquet ER, Naef F (2019), Low-dimensional dynamics of two coupled biological oscillators. *Nature Physics.* 1086–1094.

El Cheikh R, Bernard S, El Khatib N (2014), Modeling circadian clock-cell cycle interaction effects on cell population growth rates. *Journal of Theoretical Biology.* 318–331.

Elowitz MB, Levine AJ, Siggia ED, Swain PS (2002), Stochastic gene expression in a single cell. *Science (New York, N.Y.).* 1183–1186.

Feillet C, van der Horst GTJ, Rand DA, Delaunay F (2015), Coupling between the Circadian Clock and Cell Cycle Oscillators: Implication for Healthy Cells and Malignant Growth. *Frontiers in Neurology.*

Ferro A, Mestre T, Carneiro P, Sahumbaiev I, Seruca R, Sanches JM (2017), Blue intensity matters for cell cycle profiling in fluorescence DAPI-stained images. *Laboratory Investigation.* 615–625.

Friesen WO, Block GD (1984), What is a biological oscillator? *American Journal of Physiology-Regulatory, Integrative and Comparative Physiology.* R847–R853.

Gaucher J, Montellier E, Sassone-Corsi P (2018), Molecular Cogs: Interplay between Circadian Clock and Cell Cycle. *Trends in Cell Biology.* 368–379.

Goldbeter A (1995), A model for circadian oscillations in the Drosophila period protein (PER). *Proceedings. Biological Sciences.* 319–324.

Granada AE, Bordyugov G, Kramer A, Herzel H (2013), Human Chronotypes from a Theoretical Perspective. *PLOS ONE.* e59464.

Gérard C, Goldbeter A (2009), Temporal self-organization of the cyclin/Cdk network driving the mammalian cell cycle. *Proceedings of the National Academy of Sciences.* 21643–21648.

Hara M, Abe Y, Tanaka T, Yamamoto T, Okumura E, Kishimoto T (2012), Greatwall kinase and cyclin B-Cdk1 are both critical constituents of M-phase-promoting factor. *Nature Communications.* 1059.

Harper E, Talbot CJ (2019), Is it Time to Change Radiotherapy: The Dawning of Chronoradiotherapy? *Clinical Oncology.* 326–335.

Hastings MH, Maywood ES, Brancaccio M (2018), Generation of circadian rhythms in the suprachiasmatic nucleus. *Nature Reviews Neuroscience.* 453–469.

Hrushesky WJM (1985), Circadian Timing of Cancer Chemotherapy. *Science.* 73–75.

Jiang W, Zhao S, Jiang X, Zhang E, Hu G, Hu B, Zheng P, Xiao J, Lu Z, Lu Y, Ni J, Chen C, Wang X, Yang L, Wan R (2016), The circadian clock gene *Bmal1* acts as a potential anti-oncogene in pancreatic cancer by activating the p53 tumor suppressor pathway. *Cancer Letters.* 314–325.

Kapiteijn E, Marijnen CA, Nagtegaal ID, Putter H, Steup WH, Wiggers T, Rutten HJ, Pahlman L, Glimelius B, van Krieken JH, Leer JW, van de Velde CJ, Dutch Colorectal Cancer Group (2001), Preoperative radiotherapy combined with total mesorectal excision for resectable rectal cancer. *The New England Journal of Medicine.* 638–646.

Kiessling S, Beaulieu-Laroche L, Blum ID, Landgraf D, Welsh DK, Storch KF, Labrecque N, Cermakian N (2017), Enhancing circadian clock function in cancer cells inhibits tumor growth. *BMC Biology.* 13.

Ko CH, Takahashi JS (2006), Molecular components of the mammalian circadian clock. *Human Molecular Genetics.* R271–R277.

Kowalska E, Ripperger JA, Hoegger DC, Bruegger P, Buch T, Birchler T, Mueller A, Albrecht U, Contaldo C, Brown SA (2013), NONO couples the circadian clock to the cell cycle. *Proceedings of the National Academy of Sciences.* 1592–1599.

Kuramoto Y (1984), Chemical Oscillations, Waves, and Turbulence. Springer.

Lee Y (2021), Roles of circadian clocks in cancer pathogenesis and treatment. *Experimental & Molecular Medicine.* 1529–1538.

Lee YJ, Kang YR, Lee SY, Jin Y, Han DC, Kwon BM (2017), Ginkgetin induces G2-phase arrest in HCT116 colon cancer cells through the modulation of b-Myb and miRNA34a expression. *International Journal of Oncology.* 1331–1342.

Leloup JC, Goldbeter A (2004), Modeling the mammalian circadian clock: Sensitivity analysis and multiplicity of oscillatory mechanisms. *Journal of Theoretical Biology.* 541–562.

Liu AC, Tran HG, Zhang EE, Priest AA, Welsh DK, Kay SA (2008), Redundant Function of REV-ERB and and Non-Essential Role for Bmal1 Cycling in Transcriptional Regulation of Intracellular Circadian Rhythms. *PLOS Genetics.* e1000023.

Liu J, Clough SJ, Hutchinson AJ, Adamah-Biassi EB, Popovska-Gorevski M, Dubocovich ML (2016), MT $_1$ and MT $_2$ Melatonin Receptors: A Therapeutic Perspective. *Annual Review of Pharmacology and Toxicology.* 361–383.

Lévi F (2002), From circadian rhythms to cancer chronotherapeutics. *Chronobiology International.* 1–19.

Lévi F, Zidani R, Misset JL (1997), Randomised multicentre trial of chronotherapy with oxaliplatin, fluorouracil, and folinic acid in metastatic colorectal cancer. *The Lancet.* 681–686.

Maier P, Hartmann L, Wenz F, Herskind C (2016), Cellular Pathways in Response to Ionizing Radiation and Their Targetability for Tumor Radiosensitization. *International Journal of Molecular Sciences.* 102.

Matsuo T, Yamaguchi S, Mitsui S, Emi A, Shimoda F, Okamura H (2003), Control Mechanism of the Circadian Clock for Timing of Cell Division in Vivo. *Science.* 255–259.

Miki T, Matsumoto T, Zhao Z, Lee CC (2013), p53 regulates Period2 expression and the circadian clock. *Nature Communications.* 2444.

Miller EM, Fowler JF, Kinsella TJ (1992), Linear-quadratic analysis of radiosensitization by halogenated pyrimidines. I. Radiosensitization of human colon cancer cells by iododeoxyuridine. *Radiation Research.* 81–89.

Mirsky HP, Liu AC, Welsh DK, Kay SA, Doyle FJ (2009), A model of the cell-autonomous mammalian circadian clock. *Proceedings of the National Academy of Sciences.* 11107–11112.

Novak B, Pataki Z, Ciliberto A, Tyson JJ (2001), Mathematical model of the cell division cycle of fission yeast. *Chaos: An Interdisciplinary Journal of Nonlinear Science.* 277–286.

Okazaki H, Matsunaga N, Fujioka T, Okazaki F, Akagawa Y, Tsurudome Y, Ono M, Kuwano M, Koyanagi S, Ohdo S (2014), Circadian Regulation of mTOR by the Ubiquitin Pathway in Renal Cell Carcinoma. *Cancer Research.* 543–551.

Oklejewicz M, Destici E, Tamanini F, Hut RA, Janssens R, Van Der Horst GT (2008), Phase Resetting of the Mammalian Circadian Clock by DNA Damage. *Current Biology.* 286–291.

Ozbudak EM, Thattai M, Kurtser I, Grossman AD, van Oudenaarden A (2002), Regulation of noise in the expression of a single gene. *Nature Genetics.* 69–73.

Papagiannakopoulos T, Bauer M, Davidson S, Heimann M, Subbaraj L, Bhutkar A, Bartlebaugh J, Vander Heiden M, Jacks T (2016), Circadian Rhythm Disruption Promotes Lung Tumorigenesis. *Cell Metabolism.* 324–331.

Pawlik TM, Keyomarsi K (2004), Role of cell cycle in mediating sensitivity to radiotherapy. *International Journal of Radiation Oncology*Biology*Physics.* 928–942.

Pereira PD, Serra-Caetano A, Cabrita M, Bekman E, Braga J, Rino J, Santus R, Filipe PL, Sousa AE, Ferreira JA (2017), Quantification of cell cycle kinetics by EdU (5-ethynyl-2-deoxyuridine)-coupled-fluorescence-intensity analysis. *Oncotarget.* 40514–40532.

Plikus MV, Vollmers C, De La Cruz D, Chaix A, Ramos R, Panda S, Chuong CM (2013), Local circadian clock gates cell cycle progression of transient amplifying cells during regenerative hair cycling. *Proceedings of the National Academy of Sciences.*

Powathil GG, Adamson DJA, Chaplain MAJ (2013), Towards Predicting the Response of a Solid Tumour to Chemotherapy and Radiotherapy Treatments: Clinical Insights from a Computational Model. *PLOS Computational Biology.* e1003120.

Relógio A, Westermark PO, Wallach T, Schellenberg K, Kramer A, Herzel H (2011), Tuning the Mammalian Circadian Clock: Robust Synergy of Two Loops. *PLOS Computational Biology.* e1002309.

Reyes J, Chen JY, Stewart-Ornstein J, Karhohs KW, Mock CS, Lahav G (2018), Fluctuations in p53 Signaling Allow Escape from Cell-Cycle Arrest. *Molecular Cell.* 581–591.e5.

Ruoff P, Rensing L (1996), The Temperature-Compensated Goodwin Model Simulates Many Circadian Clock Properties. *Journal of Theoretical Biology.* 275–285.

Sachs RK, Hahnfeld P, Brenner DJ (1997), The link between low-LET dose-response relations and the underlying kinetics of damage production/repair/misrepair. *International Journal of Radiation Biology.* 351–374.

Sahay S, Adhikari S, Hormoz S, Chakrabarti S (2023), An improved rhythmicity analysis method using Gaussian Processes detects cell-density dependent circadian oscillations in stem cells. *Bioinformatics.* btad602.

Shafi AA, Knudsen KE (2019), Cancer and the Circadian Clock. *Cancer Research.* 3806–3814.

Sinclair WK, Morton RA (1965), X-Ray and Ultraviolet Sensitivity of Synchronized Chinese Hamster Cells at Various Stages of the Cell Cycle. *Biophysical Journal.* 1–25.

Strogatz SH (2000), From Kuramoto to Crawford: exploring the onset of synchronization in populations of coupled oscillators. *Physica D: Nonlinear Phenomena.* 1–20.

Sulli G, Manoogian ENC, Taub PR, Panda S (2018), Training the Circadian Clock, Clocking the Drugs, and Drugging the Clock to Prevent, Manage, and Treat Chronic Diseases. *Trends in Pharmacological Sciences.* 812–827.

Takane H, Ohdo S, Yamada T, Yukawa E, Higuchi S (2000), Chronopharmacology of antitumor effect induced by interferon-beta in tumor-bearing mice. *The Journal of Pharmacology and Experimental Therapeutics.* 746–752.

Terasima T, Tolmach LJ (1961), Changes in X-ray Sensitivity of HeLa Cells during the Division Cycle. *Nature.* 1210–1211.

Tyson JJ, Novak B (2001), Regulation of the Eukaryotic Cell Cycle: Molecular Antagonism, Hysteresis, and Irreversible Transitions. *Journal of Theoretical Biology.* 249–263.

Welsh DK, Takahashi JS, Kay SA (2010), Suprachiasmatic Nucleus: Cell Autonomy and Network Properties. *Annual Review of Physiology.* 551–577.

Wheeler RJ (2015), Analyzing the dynamics of cell cycle processes from fixed samples through ergodic principles. *Molecular Biology of the Cell.* 3898–3903.

Winfree AT (1967), Biological rhythms and the behavior of populations of coupled oscillators. *Journal of Theoretical Biology.* 15–42.

Yan J, Goldbeter A (2019), Robust synchronization of the cell cycle and the circadian clock through bidirectional coupling. *Journal of The Royal Society Interface.* 20190376.

Yoo SH, Yamazaki S, Lowrey PL, Shimomura K, Ko CH, Buhr ED, Siepka SM, Hong HK, Oh WJ, Yoo OJ, Menaker M, Takahashi JS (2004), PERIOD2::LUCIFERASE real-time reporting of circadian dynamics reveals persistent circadian oscillations in mouse peripheral tissues. *Proceedings of the National Academy of Sciences.* 5339–5346.

Zhang Y, Devocelle A, Souza L, Foudi A, Bento ST, Desterke C, Sherrard R, Ballesta A, Adam R, Giron-Michel J, Chang Y (2020), BMAL1 knockdown triggers different colon carcinoma cell fates by altering the delicate equilibrium between AKT/mTOR and P53/P21 pathways. *Aging.* 8067–8083.

Zámborszky J, Hong CI, Csikász Nagy A (2007), Computational Analysis of Mammalian Cell Division Gated by a Circadian Clock: Quantized Cell Cycles and Cell Size Control. *Journal of Biological Rhythms.* 542–553.